Charmed Baryon Decays Observed in e^+e^- Annihilation at SPEAR

Eric Nelson Vella

ABSTRACT

Various weak decays of the charmed baryon Λ_c are observed in the Mark II detector at the SLAC e^+e^- storage ring SPEAR. Hadronic decays $\Lambda_c^+ \to pK^-\pi^+$ and $\Lambda_c^+ \to pK_S^0$ and their charge conjugates are observed as peaks in invariant mass spectra at $m(\Lambda_c) = (2286 \pm 5)$ MeV/c^2. An estimate of the charmed baryon production cross section, $\sigma(\Lambda_c) + \sigma(\bar{\Lambda}_c) = (1.7 \pm 0.4)$ nb, derived from Mark II measurements of the inclusive baryon cross sections R_p and R_Λ as functions of center-of-mass energy, is used to calculate branching ratios for these hadronic decays :

$$BR\ (\Lambda_c^+ \to p\ K^-\ \pi^+) = (2.0 \pm 0.8)\ \%\ ;$$

$$BR\ (\Lambda_c^+ \to p\ K_S^0) / BR\ (\Lambda_c^+ \to p\ K^-\ \pi^+) = (36 \pm 16)\ \%\ .$$

An attempt is also made to observe higher mass charmed baryons by reconstructing cascade decays $\Sigma_c \to \Lambda_c\pi$.

Evidence for the observation of semileptonic decays of the charmed baryon is presented. Direct electrons are observed in events containing antiprotons, lambdas and antilambdas. The number of electrons per baryon event, after background subtraction and efficiency correction, is used, together with an estimate of the charmed baryon content of proton and lambda events, to calculate inclusive and semi-inclusive semileptonic branching ratios of the Λ_c :

$$BR\ (\Lambda_c^+ \to e^+\ X) = (4.5 \pm 1.8)\ \%\ ;$$

$$BR\ (\Lambda_c^+ \to p\ e^+\ X) = (1.9 \pm 0.8)\ \%\ ;$$

$$BR\ (\Lambda_c^+ \to \Lambda^0\ e^+\ X) = (1.2 \pm 0.6)\ \%\ .$$

The inclusive semileptonic branching ratio, combined with a theoretical calculation of the total semileptonic width, implies a lifetime $\tau(\Lambda_c) = (2.4 \pm 1.1)\ 10^{-13}$ sec, in good agreement with recent direct measurements.

LBL--13845

DE82 005159

CHARMED BARYON DECAYS OBSERVED IN e^+e^- ANNIHILATION AT SPEAR*

Eric Nelson Vella

Department of Physics and Lawrence Berkeley Laboratory
University of California, Berkeley, California 94720

(Ph.D. Thesis)

DISCLAIMER

*Work supported by the Director, Office of Energy Research, Division of High Energy and Nuclear Physics of the U.S. Department of Energy under Contracts DE-AC03-76SF00515 and W-7405-ENG-48.

DISTRIBUT

ACKNOWLEDGEMENTS

I wish to thank the members of the SLAC-LBL Mark II collaboration whose combined efforts made the Mark II experiment at SPEAR a success. Special thanks must go to my advisor George Trilling for invaluable guidance throughout all phases of the research leading to this thesis. Finally, I would like to thank Connie Oshiro for her support and encouragement, which helped make my experience as a graduate student a pleasant one.

CONTENTS

page

1. INTRODUCTION AND CHARMED BARYON THEORY 1

Introduction 1
Charmed Baryon States 3
Charmed Baryon Decays 6

2. MARK II DETECTOR 10

Subsystems 10
Drift Chamber System 14
Time of Flight System 16
Pion - Kaon - Proton Separation by TOF 19
Liquid Argon System 22
Physical Construction 22
Electronics 25
Charge Collection 26
Calibration 27
Energy Resolution 28
Pion - Electron Separation by LA 31

3. INCLUSIVE BARYON PRODUCTION 37

4. HADRONIC DECAYS OF THE CHARMED BARYON 43

Data Sample 44
$\Lambda_c \rightarrow pK\pi$ Decay Mode 46
$\Lambda_c \rightarrow pK^0_s$ Decay Mode 52
$\Lambda_c \rightarrow \Lambda^0\pi$ Decay Mode 57
Λ_c Mass Determination 61
Higher Mass Charmed Baryons 63
Λ_c Recoil Mass 63
Σ_c Reconstruction 66

5. SEMILEPTONIC DECAYS OF THE CHARMED BARYON 70

Data Sample 71
Baryon Identification 72
Event Selection 78
Calculation of Electron Signal 82
Electron Identification Procedure 83
Electron Identification Efficiency 89
Charged Pion Misidentification 93
Electron - Positron Pairs from Pizero Decay 98
Results 101
Electron Signal 101
Electron Momentum Spectrum 106
E_{cm} Distribution of Electron Events 110
Electrons per Baryon Event 112
Semileptonic Branching Ratios 113

Λ_c lifetime 116

REFERENCES 117

LIST OF TABLES

Table page

1. Ground state ($J^P = \frac{1}{2}^+$) charmed baryons 4
2. Material preceding drift chamber exit 13
3. LA channel ganging scheme 25
4. Inclusive proton and lambda production 40
5. Baryon event samples 72
6. Electron detection efficiency 91
7. Pion misidentification probability for $p < 300$ MeV/c 94
8. Pion misidentification probability for $p > 300$ MeV/c 96
9. Electron signal 9992 $\bar{p}$ events $E_{cm} < 4.5$ GeV 102
10. Electron signal 5209 $\bar{p}$ events $E_{cm} > 4.5$ GeV 103
11. Electron signal 1667 $\Lambda^0 + \bar{\Lambda}^0$ events $E_{cm} < 4.5$ GeV 104
12. Electron signal 837 $\Lambda^0 + \bar{\Lambda}^0$ events $E_{cm} > 4.5$ GeV 105
13. Electron momentum spectra $E_{cm} > 4.5$ GeV 106
14. E_{cm} distribution of electron events 110
15. $\Delta R_p / R_p$ and $\Delta R_\Lambda / R_\Lambda$ 114

LIST OF FIGURES

Figure		page
1.	Weight diagram for $J^P = \frac{1}{2}^+$ charmed baryons	5
2.	Quark diagrams for Λ_c^+ decay	8
3.	Mark II detector at SPEAR	11
4.	Time of flight resolution	18
5.	Particle identification by time-of-flight	20
6.	Liquid argon cell geometry and readout scheme	24
7.	LA energy resolution for electrons	30
8.	LA energy deposition by electrons and pions	34
9.	Inclusive proton and lambda production	41
10.	Vertex distributions for proton - kaon events	45
11.	$pK\pi$ invariant mass distributions	48
12.	$\Lambda_c \to pK\pi$ detection efficiency	50
13.	$\pi^+\pi^-$ invariant mass spectrum in proton events	53
14.	pK_S^0 invariant mass distributions	55
15.	$\Lambda_c \to pK_S^0$ detection efficiency	56
16.	$\Lambda^0\pi$ invariant mass distribution	58
17.	$\Lambda_c \to \Lambda^0\pi$ detection efficiency	59
18.	$pK\pi$ plus pK_S^0 invariant mass distribution	62
19.	$pK\pi$ plus pK_S^0 recoil mass distributions	64
20.	Equal recoil invariant mass distribution	65
21.	$\Sigma_c - \Lambda_c$ mass difference	69
22.	Proton identification by TOF	74
23.	$\bar{p}\pi^+$ and $p\pi^-$ invariant mass spectra	76
24.	Proton and lambda detection efficiencies	77

25. Primary vertex Z_V distributions 79

26. $p\pi^-$ invariant mass spectra with charge cut 81

27. $(t-t_\pi)$ vs. $(t-t_e)$ for pions and electrons 86

28. Liquid argon energy vs. momentum 88

29. Electron detection efficiency 92

30. Pion misidentification probabilities 97

31. Electron momentum spectra $E_{cm} > 4.5$ GeV 109

32. E_{cm} distribution of electron events 111

1. INTRODUCTION AND CHARMED BARYON THEORY

1.1 INTRODUCTION

Charmed baryons analyzed in this thesis were produced in e^+e^- annihilation at the Stanford Linear Accelerator Center (SLAC) e^+e^- storage ring SPEAR. Charmed baryon decays were observed in the Mark II detector at SPEAR in data taken at center-of-mass energies from 4.5 to 6.8 GeV. Most of the results presented in the following chapters are observations of various weak decays of the charmed baryon Λ_c.

Chapter 1 presents some important aspects of the theory of charmed baryons, including the expected spectrum of charmed baryon states and the most likely hadronic and semileptonic decay modes of charmed baryons. The Mark II detector and particle identification techniques are described in chapter 2. Chapter 3 presents data on inclusive proton and lambda production in e^+e^- annihilation at SPEAR energies, from which an estimate of the charmed baryon production cross section can be made. Chapter 4 presents observations of hadronic decays of the charmed baryon Λ_c. The decay modes $\Lambda_c^+ \to pK^-\pi^+$ and $\Lambda_c^+ \to pK_S^0$ are observed and branching ratios are calculated. An attempt is also made to reconstruct higher mass charmed baryons which decay strongly to the Λ_c by pion emission. Chapter 5 presents the first evidence for the observation of semileptonic decays of charmed baryons. A direct electron signal seen in proton and lambda events at energies above the threshold

for charmed baryon pair production is used to calculate several inclusive and semi-inclusive semileptonic branching ratios of the Λ_c.

1.2 CHARMED BARYON STATES

Charmed baryons fit naturally into the framework of the quark model with the inclusion of the charmed quark [1] . The ground state ($J^P = \frac{1}{2}^+$) charmed baryons are bound states of three quarks, with wave functions symmetric in spatial coordinates and antisymmetric in color indices. By the generalized Pauli principle, they must be symmetric under the simultaneous interchange of spin and flavor (quark label u,d,s,c) of any pair of quarks. Altogether 20 such states may be constructed out of the four quarks u,d,s,c. These 20 states form an irreducible representation of the group SU(4). The SU(4) weight diagram for these states is shown in figure 1.

Uncharmed baryons form an SU(3) octet. Singly charmed baryons, containing one c quark, may be either symmetric or antisymmetric in the remaining two quarks. The symmetric combinations form an SU(3) sextuplet and the antisymmetric combinations form an SU(3) triplet. Doubly charmed baryons, containing two c quarks, form an SU(3) triplet in the remaining quark. Names, quark content, quantum numbers, and mass estimates [2] of the ground state charmed baryons are collected in table 1.

TABLE 1

Ground state ($J^P = \frac{1}{2}^+$) charmed baryons

name(s)	quark content	SU(3)	C	S	Y	I	I_3	mass est. (GeV/c^2)
Λ_c^+ (C_0^+)	$c(ud)_a$	$\bar{3}$	1	0	0	0	0	2.26
Σ_c^{++} (C_1^{++})	cuu	6	1	0	0	1	+1	2.42
Σ_c^+ (C_1^+)	$c(ud)_s$	6	1	0	0	1	0	2.42
Σ_c^0 (C_1^0)	cdd	6	1	0	0	1	-1	2.42
Ξ_c^{A+} (A^+)	$c(su)_a$	$\bar{3}$	1	-1	-1	$\frac{1}{2}$	$+\frac{1}{2}$	2.47
Ξ_c^{A0} (A^0)	$c(sd)_a$	$\bar{3}$	1	-1	-1	$\frac{1}{2}$	$-\frac{1}{2}$	2.47
Ξ_c^+ (S^+)	$c(su)_s$	6	1	-1	-1	$\frac{1}{2}$	$+\frac{1}{2}$	2.56
Ξ_c^0 (S^0)	$c(sd)_s$	6	1	-1	-1	$\frac{1}{2}$	$-\frac{1}{2}$	2.56
Ω_c (T^0)	css	6	1	-2	-2	0	0	2.73
Ξ_{cc}^+ (X_u^+)	ccu	3	2	0	-1	$\frac{1}{2}$	$+\frac{1}{2}$	3.61
Ξ_{cc}^0 (X_d^0)	ccd	3	2	0	-1	$\frac{1}{2}$	$-\frac{1}{2}$	3.61
Ω_{cc} (X_s^+)	ccs	3	2	-1	-2	0	0	3.79

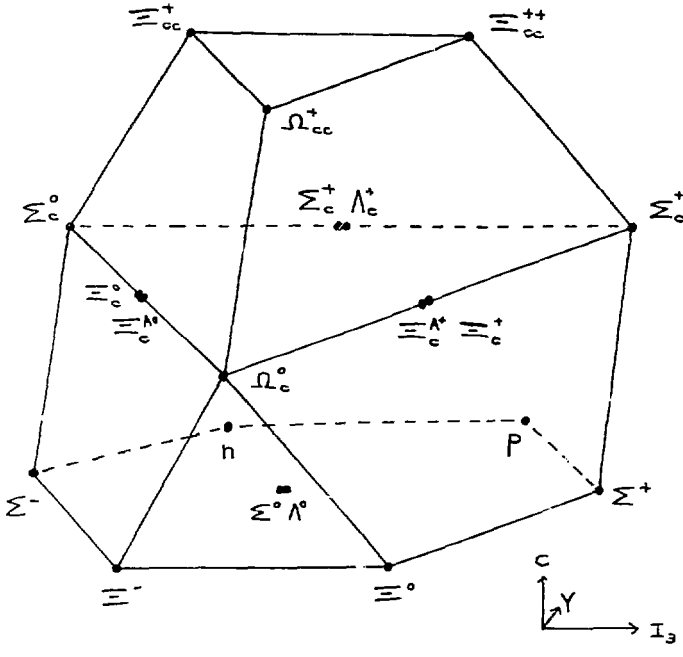

Figure 1: Weight diagram for $J^P = \frac{1}{2}^+$ charmed baryons

1.3 CHARMED BARYON DECAYS

The Λ_c is the lightest charmed baryon (the relationship $m_{\Lambda_c} < m_{\Sigma_c} < m_{\Xi_c}$ follows from the relationship $m_\Lambda < m_\Sigma < m_\Xi$ for uncharmed baryons) and cannot decay into any other charmed final state (since the decay $\Lambda_c \rightarrow$ (baryon) + (charmed meson) is kinematically forbidden). Since strong and electromagnetic interactions conserve charm, the Λ_c must decay weakly.

Charmed baryons more massive than the Λ_c may be able to decay strongly to lower lying charmed baryons. Strong decays between charmed baryons of the same strangeness will proceed by pion emission, provided the mass differences are greater than the pion mass [3]. The decay $\Sigma_c \rightarrow \Lambda_c\pi$, in particular, has been observed in several neutrino experiments [4], with a mass difference $m(\Sigma_c) - m(\Lambda_c) = (168 \pm 3)$ MeV/c^2 near the theoretical value of 160 MeV/c^2.

Weak decays of the Λ_c proceed via current - current interactions, mediated by W boson exchange. In the standard GIM model [5], the hadronic and leptonic weak charged currents are given by

$$J^\alpha_H = \bar{u}\,\gamma^\alpha(1-\gamma_5)\,(d\cos\theta_c + s\sin\theta_c) + \bar{c}\,\gamma^\alpha(1-\gamma_5)\,(s\cos\theta_c - d\sin\theta_c)$$

$$J^\alpha_L = \bar{\nu}_e\,\gamma^\alpha(1-\gamma_5)\,e + \bar{\nu}_\mu\,\gamma^\alpha(1-\gamma_5)\,\mu$$

Neutral weak currents also exist, but do not give rise to charm changing interactions.

Since the Cabibbo angle θ_c is small ($\sin^2\theta_c \approx .05$), the c quark decays predominantly into an s quark. Nonstrange charmed baryons will

thus decay predominantly into final states containing a strange particle. Quark model diagrams for Λ_c^+ decay via the Cabibbo favored weak charged currents are shown in figure 2. Figure 2(a) shows the standard Cabibbo allowed decay $c \to s u \bar{d}$, with the light quarks in the charmed baryon acting as spectators. Figure 2(b) is a non-spectator diagram showing the $cd \to su$ transition. Figure 2(c) shows the semileptonic decay of the charmed baryon proceeding via the quark decay $c \to s \ell^+ \nu_\ell$.

The decay rates and hence lifetimes of charmed particles can be estimated roughly by comparing the diagrams for the quark decays $c \to s u \bar{d}$ and $c \to s \bar{\ell} \nu_\ell$ to the analogous diagram for muon decay $\mu \to e \nu \bar{\nu}$. Since the muon decay rate is proportional to m_μ^5 and there are five times as many final states for c quark decay as for μ decay (three colors for $u\bar{d}$ and two lepton types for $\bar{\ell} \nu_\ell$), the result is

$$\Gamma_c \simeq 5\ (m_c/m_\mu)^5\ \Gamma_\mu$$

$$\simeq 2 \cdot 10^{-3}\ \text{eV} \simeq 3 \cdot 10^{12}\ \text{sec}^{-1} \qquad (\text{for } m_c = 1.75\ \text{GeV}/c^2).$$

This decay width is negligible in comparison with any experimental resolution. The corresponding lifetime implies a decay distance ($c\tau$) on the order of a tenth of a millimeter, much shorter than can be seen with the Mark II detector.

The relative importance of semileptonic decays of charmed particles can be estimated by the same final state counting argument given above. A semileptonic branching ratio of 20 % (to e or μ) results. This is an overestimate of the actual branching ratios observed in semileptonic decays of charmed mesons [6], and is almost certainly an overestimate for charmed baryon semileptonic decays also. (The non-spectator diagram $cd \to su$ is neglected, and there is known to be a considerable en-

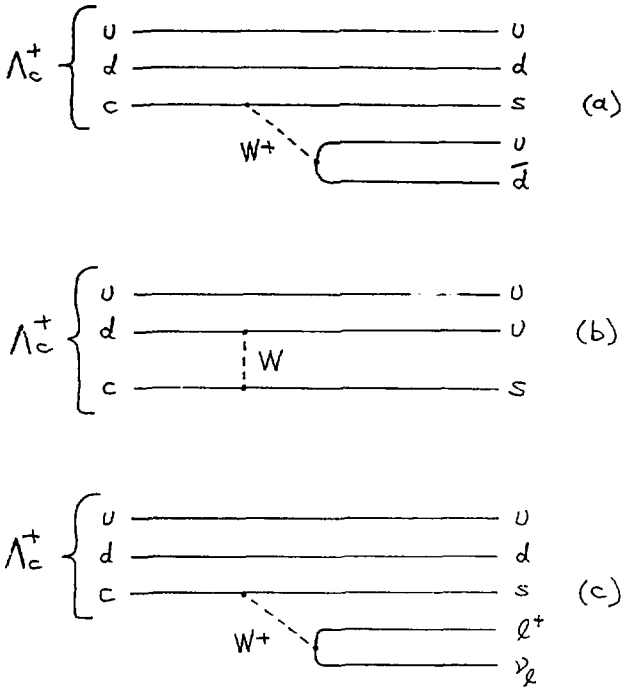

Figure 2: Quark diagrams for Λ_c^+ decay

(a) hadronic decays (spectator diagram)
(b) hadronic decays (non-spectator diagram)
(c) semileptonic decays

hancement of hadronic final states in the analogous case of strange baryon decay.)

After final state interactions, the various quarks produced in Λ_c^+ decay can form a large number of possible final states. In purely hadronic decays, possible two-body final states include $p\bar{K}^0$, $\Lambda^0\pi^+$, $\Sigma^0\pi^+$, $\Sigma^+\pi^0$, Ξ^0K^+, $\Delta^{++}K^-$, and $\Delta^+\bar{K}^0$ [7]. Multibody final states, including $pK^-\pi^+$ and other states with extra pions, may also be important [8]. In semileptonic decays of the Λ_c^+, the simplest final state is $\Lambda^0\ell^+\nu_\ell$ (ℓ = e or μ). The final state $n\ell^+\nu_\ell$ is also possible (though Cabibbo forbidden) and may contribute at a lower level [9]. Higher multiplicity final states such as $pK^-\ell^+\nu_\ell$ and $\Sigma^+\pi^-\ell^+\nu_\ell$ may also have substantial (though smaller) decay rates [10] .

2. MARK II DETECTOR

2.1 SUBSYSTEMS

The Mark II detector at SPEAR was a general purpose cylindrically symmetric magnetic detector, consisting of the following elements (proceeding radially outward from the e^+e^- beam axis) :

1) beam pipe and pipe counter
2) drift chamber (DC)
3) time-of-flight (TOF) counters
4) magnet coil
5) liquid argon (LA) calorimeters
6) muon system

The endcap regions at SPEAR were also instrumented, with a proportional chamber on one side and a liquid argon endcap on the other side.

Figure 3 shows two views of the detector and its various subsystems. In this chapter, the drift chamber, the time-of-flight system, and the liquid argon system will be described in some detail. The muon system and the endcaps are not relevant to the analysis presented in later chapters and will not be discussed here.

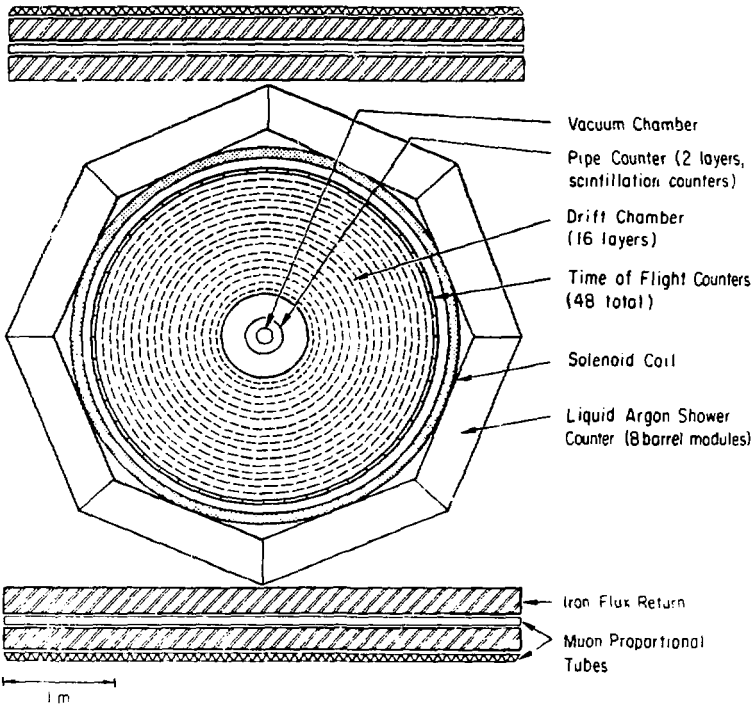

(a) Cross sectional view of the Mark II detector.

Figure 3: Mark II detector at SPEAR

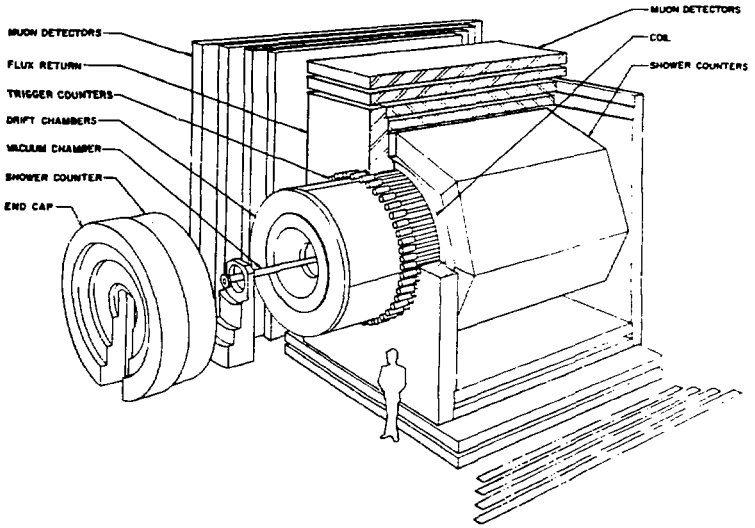

(b) Expanded isometric view of the Mark II detector.

Figure 3: Mark II detector at SPEAR

The amount of material encountered by a particle travelling from the e^+e^- interaction point through the drift chamber system is shown in table 2.

TABLE 2

Material preceding drift chamber exit

	radius (cm)	thickness (g/cm^2)	E loss (MeV)	radiation lengths
vaccuum chamber	8	0.16	0.2	.012
pipe counter	12	1.57	3.0	.038
lexan window	37	0.38	0.7	.009
DC gas + wires	40-140	0.21	0.5	.009

2.2 DRIFT CHAMBER SYSTEM

A complete and detailed description of the Mark II drift chamber (DC) system may be found in the PhD thesis of Rafe Schindler [11] , and only the essentials will be presented here.

The drift chamber at SPEAR consisted of 16 concentric cylindrical layers of wires enclosed in a common gas volume. The wire layers surrounded the e^+e^- beam axis at radii of 0.4 to 1.4 m and were 2.0 to 2.8 m in length. Six layers were strung with wires parallel to the beam axis and magnetic field; ten layers were strung with wires at $\pm 3^0$ stereo angles to this axis (to provide axial position measurements). The overall solid angle coverage of the DC system was 85 % of 4π.

Charged particles passing through the drift chamber deposited tracks of ionization in the drift chamber gas (a mixture of argon and ethane). Sets of electric field shaping wires in each drift chamber layer caused this ionization to drift (with drift velocity 50 μm/ns) toward central sense wires, where the induced signals were read out electronically. The drift time for each hit wire was digitized and recorded along with the wire azimuth and layer number. In the offline analysis (and also online, with a few modifications), tracks were reconstructed by converting the drift times to drift distances and then fitting sets of hits to helical trajectories through the successive drift chamber layers.

The drift chamber spatial resolution was approximately 200 μm. For a typical charged particle path length of 1 meter in the drift chamber, this gave an intrinsic transverse momentum ($p_\perp$) resolution of $(\delta p_\perp/p_\perp) \approx 1\%\ p_\perp$ ($p_\perp$ in GeV/c). Multiple scattering in the material

(gas and wires) within the drift chamber volume added a constant error of $(\delta p_\perp/p_\perp) \simeq 1.5\%$ to this resolution. The overall transverse momentum resolution was thus given by

$$(\delta p_\perp/p_\perp) \simeq \sqrt{(1.5\%)^2 + (1.0\%\ p_\perp)^2} \qquad (p_\perp \text{ in GeV/c}) \ .$$

After all charged tracks in an event were reconstructed, a primary vertex was defined by fitting as many tracks as possible to a common origin near the known e^+e^- beam interaction point. Tracks passing within a small region about the interaction point (1.5 cm in the radial direction and 15 cm in the longitudinal direction) were refitted with the requirement that they pass through the same interaction point. This 'beam constrained' fit reduced the intrinsic momentum error of the track by effectively increasing the track path length. The transverse momentum resolution for beam constrained tracks was given by

$$(\delta p_\perp/p_\perp) \simeq \sqrt{(1.5\%)^2 + (0.5\%\ p_\perp)^2} \qquad (p_\perp \text{ in GeV/c}) \ .$$

2.3 TIME OF FLIGHT SYSTEM

The time-of-flight (TOF) system of the Mark II detector consisted of 48 plastic scintillators surrounding the drift chamber at a radius of 1.5 m. Each scintillator was 25 mm thick, 20 cm wide, and 3.4 m long. The scintillators were viewed at each end by 2" photomultipliers whose output (both arrival time and pulseheight) was digitized and recorded. The overall solid angle coverage of the TOF system was 75 % of 4π.

The time-of-flight of a particle was calculated from the average of the two pulse arrival times recorded by the phototubes mounted on opposite ends of the scitntillator. A pulseheight slewing correction was made to correct for the effect of pulseheight variations on the measured time-of-flight. The position of the track along the length of the scintillator was also calculated (from the difference between the two pulse arrival times) and compared with the projected position of the corresponding drift chamber track.

Calibration of the TOF system was performed several times daily by 'flashing' each scintillator with pulses of light transmitted from a N_2 flashtube through a fiber optics probe attached to the center of the scintillator. This calibration was used to correct timing differences between the different phototubes and to monitor their response. Off-line calibration of the TOF system was also performed by minimizing the difference between the measured and predicted times-of-flight for reconstructed Bhabha and muon pair events.

The overall resolution of the TOF system for good tracks (single hits near the projected drift chamber position) was 300 ps. Figure 4 plots the difference between the measured and predicted times-of-flight

for a sample of low momentum (200-300 MeV/c) pions taken from reconstructed ψ' decays ($\psi' \to \psi\pi^+\pi^-$) . A Gaussian fit with resolution σ = 300 ps reproduces the data quite well.

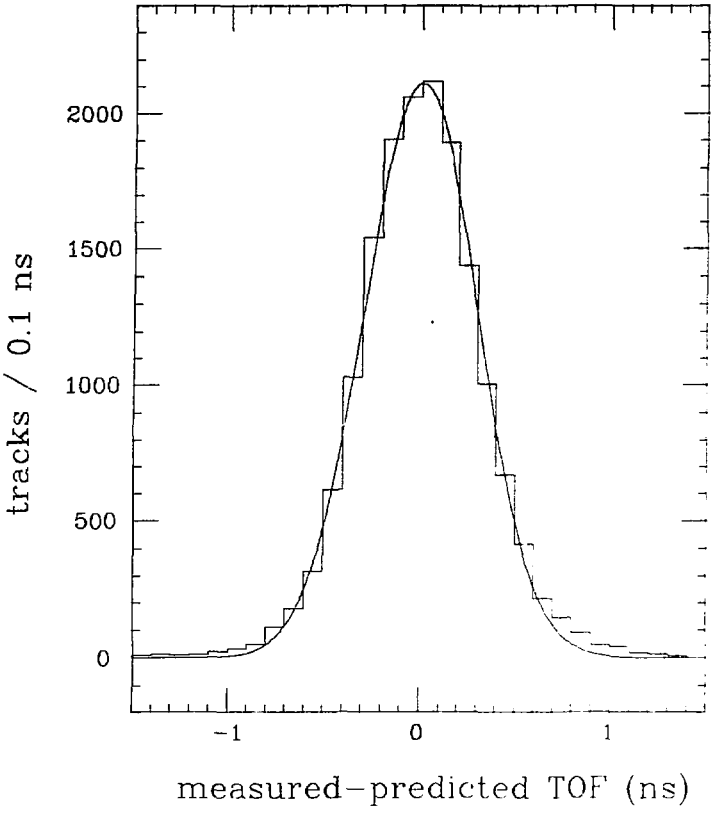

Figure 4: Time of flight resolution

TOF (measured - predicted) for 200-300 MeV/c pions

2.4 PION - KAON - PROTON SEPARATION BY TOF

The measured time-of-flight of a particle (t) was used in conjunction with the drift chamber determined path length (ℓ) and momentum (p) to identify the particle. The mass squared of the particle is calculated from these quantities as

$$m^2 = p^2 \left[(c/\ell)^2 t^2 - 1 \right] \qquad \text{with error}$$

$$\delta m^2 = 2 p \sqrt{p^2 + m^2} (c/\ell) \delta t$$

The error (δm^2) in the calculated value of m^2 increases rapidly with increasing particle momentum. For a time-of-flight resolution δt = 300 ps and a typical path length ℓ = 1.5 m , TOF separation of pions and electrons is possible up to about 300 MeV/c, TOF separation of pions and kaons is possible up to about 1.4 GeV/c, and TOF separation of kaons and protons is possible up to about 2.0 GeV/c .

TOF separation of real pions, kaons, and protons is illustrated in figure 5, a scatterplot of momentum vs mass squared. Tracks plotted in figure 5 were taken from events at center-of-mass energies from 4.5 to 6.8 GeV containing at least one proton (with proton weight greater than 0.7 as discussed below), resulting in a much larger proton concentration than would be found in an unbiased selection of events. The spreading and eventual merging of the bands of pions, kaons, and protons with increasing momentum is clearly illustrated.

To actually identify particles by time-of-flight in the following chapters, a weighting technique was used in place of a straight cut on the calculated mass. For each particle mass hypothesis (m_π, m_K, m_p), the

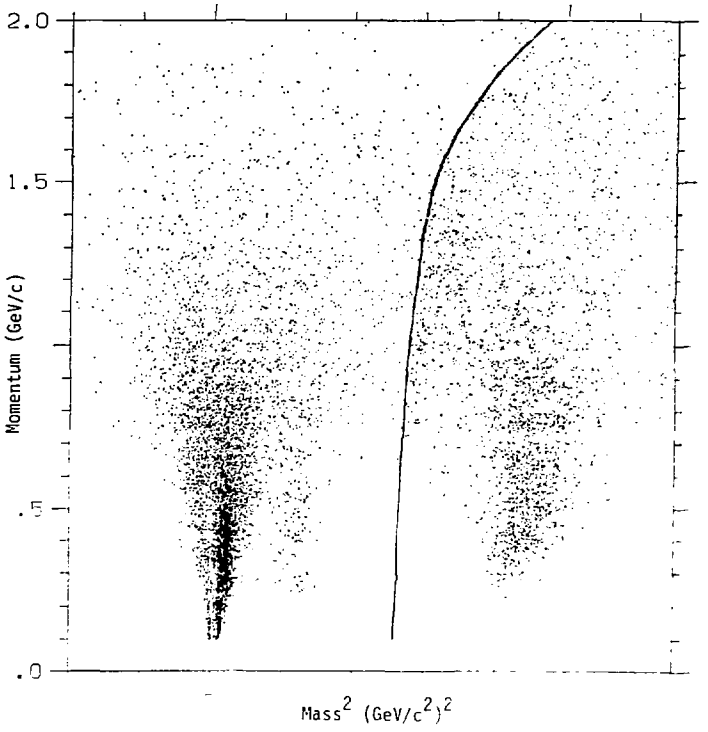

Figure 5: Particle identification by time-of-flight

tracks from proton events at E_{cm} = 4.5 - 6.8 GeV
solid curve marks boundary at TOF proton weight = 0.7

difference between the measured and predicted time-of-flight was calculated (in units of the TOF resolution σ). The weight for each hypothesis was then taken as the Gaussian amplitude for observing the calculated time-of-flight deviation. Finally, all of the weights were normalized to a sum of unity. An analogous procedure was followed to calculate an electron weight under the (m_e, m_π) hypotheses. In equations, the weighting procedure is

$$t_\pi = (\ell/c)\sqrt{1 + m_\pi^2/p^2} \qquad (t_\pi = \text{predicted TOF for } \pi)$$

$$x_\pi = (t - t_\pi)/\sigma \qquad (\sigma = \text{TOF resolution 300 ps})$$

$$W_\pi = N \exp(-\tfrac{1}{2}x_\pi^2) \qquad (W_\pi = \text{TOF pion weight})$$

$$N \text{ determined by } W_\pi + W_K + W_p = 1$$

In most of the analysis in the following chapters, protons were identified as particles with $W_p > 0.5$ or 0.7 and $p < 2.0$ GeV/c and kaons were identified as particles with $W_K > 0.5$ and $p < 1.4$ GeV/c . Increasing the weight cut used to identify a particular particle reduces contamination due to misidentification of other particles, but also lowers the efficiency for correct identification, especially at high momenta. The solid curve in figure 5 represents the cut $W_p = 0.7$ as a momentum dependent mass squared cut separating protons from pions and kaons.

2.5 LIQUID ARGON SYSTEM

The liquid argon (LA) system of the Mark II detector consisted of 8 lead - liquid argon calorimeter modules surrounding the magnet coil at a radius of about 1.8 m. Each module was 30 cm thick, 1.8 m wide, and 3.8 m long. The overall solid angle coverage of the LA system was 64 % of 4π.

A liquid argon module consisted basically of planes of lead separated by gaps of liquid argon. Electrons and photons passing through a module generated electromagnetic showers by repeated bremsstrahlung and pair production in the lead. Ionization of liquid argon in the gaps between the lead planes was used to sample the shower development and hence determine the energy of the incident electron or photon.

2.5.1 Physical Construction

Each liquid argon module had the following physical arrangement :

1) a 'trigger' section, consisting of 3 aluminum planes (1.6 mm thick) separated by 8 mm liquid argon gaps;

2) a 'lead stack', consisting of 37 lead planes (2 mm thick) separated by 3 mm liquid argon gaps.

The trigger gaps were used to measure the ionization at the entrance of the LA module, before the initiation of an electromagnetic shower in the lead stack. Showers initiated in the 1.4 radiation lengths of material (primarily the magnet coil) preceding the LA system represented an energy loss which could not be sampled in the module; the trigger gaps were used to make a correction for this loss based on a good initial ionization measurement. The main lead stack was used to measure

the total energy deposited by a particle as a function of position and depth within the module.

The lead planes and liquid argon gaps in the main stack were grouped into 18 cells, each consisting of the top half of a solid lead plane, a liquid argon gap, a segmented lead plane, a liquid argon gap, and the bottom half of a solid lead plane, as shown in figure 6(a). The aluminum trigger planes and liquid argon gaps located in front of the main lead stack comprised another similar cell.

The central (readout) plane in each cell was divided into strips to provide spatial information. Three types of strips were used —

1) 'F' strips, running parallel to the beam direction (hence measuring the azimuthal angle ϕ), 3.8 cm in width;

2) 'T' strips, running perpendicular to the F strips (hence measuring the polar angle θ), 3.8 cm in width;

3) 'U' strips, running at 45^0 angles to the F and T strips, 5.4 cm in width.

Strips of a given type were ganged together in depth (to reduce the number of channels of readout electronics needed) according to the scheme shown in table 3.

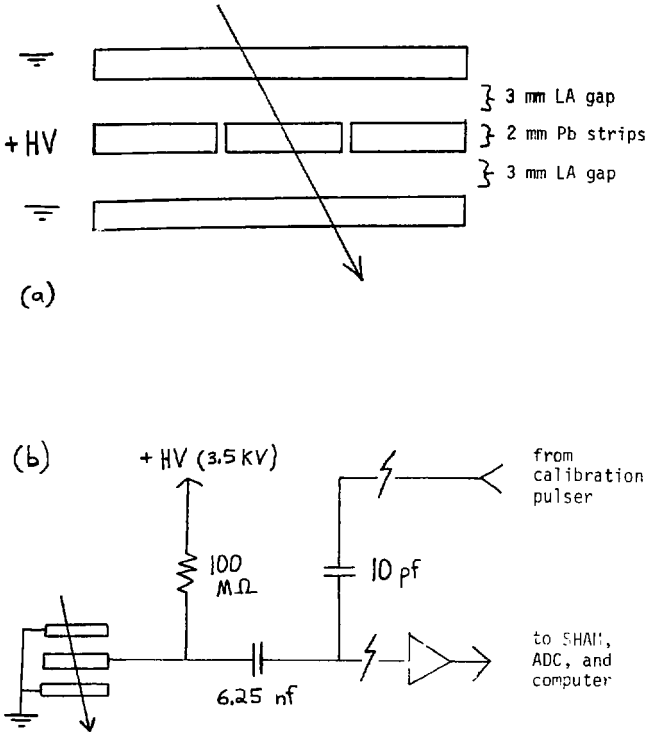

Figure 6: Liquid argon cell geometry and readout scheme

(a) LA cell geometry
(b) signal readout and calibration scheme

TABLE 3

LA channel ganging scheme

cell depth	strip type	ganging scheme	(channels)
0	F (trigger)	TR	(36)
1	F	F1	(38)
2	T	T1	(100)
3	U	U	(56)
4	F		
5	T		
6	U		
7	F		
8	T		
9	U		
10	F	F2	(40)
11	T		
12	T	T2	(52)
13	T		
14	F		
15	F		
16	F	F3	(40)
17	F		
18	F		

2.5.2 Electronics

The solid top and bottom planes of each cell were held at ground potential. Positive high voltage (generally 10 kV for the trigger cell and 3.5 kV for the lead cells) was applied to each strip in the central plane through a separate 100 MΩ resistor (so that a short in one channel would not affect other channels). The resulting electric field caused negative ions (produced in the liquid argon by the passage of charged particles) to drift toward the central readout strips. The

charge pulse induced on a strip was collected on a high voltage blocking capacitor (mounted next to the strip insiide the LA module), amplified by a preamplifier and pulse shaper (mounted on the outside of the LA module), and read out under computer control by a sample and hold module, ADC, and microprocessor (located in an electronics trailer). A sketch of this readout scheme is given in figure 6(b).

Because the ionization produced by the passage of a charged particle was collected on the readout strips without amplification, the signal to be detected was quite small, on the order of 1 picoCoulomb for a several GeV shower. A charge sensitive, low noise preamplifier with an FET input was used to amplify the signal to the several volt level. Electronics noise was a significant problem, limiting the ability of the system to distinguish low energy (100 - 200 MeV) photons from random noise fluctuations.

2.5.3 Charge Collection

A complete electromagnetic shower develops in a LA module within a few ns. Ionization electrons produced in the liquid argon gaps drift toward the readout strips with a velocity of 5 mm/μs, inducing a charge on the strips which grows with time until all the electrons are collected. Positive ions drift much more slowly and do not contribute to the measured signal. For uniform ionization across a liquid argon gap (3 mm), the induced signal rises quadratically, reaching 3/4 of its maximum value in the time it takes an electron to drift halfway across the gap (300 ps). The maximum charge induced on a strip is half the total charge of the ionization electrons [12] .

The signal produced in a single LA cell by the passage of a minimum ionizing particle is easily calculated. A minimum ionizing particle loses energy at a rate dE/dx = 2.2 MeV/cm in liquid argon. The ionization energy of liquid argon is 26 eV, so $8.5 \cdot 10^4$ ion pairs/cm are formed along the particle's track. In the 6 mm of liquid argon per cell, $5 \cdot 10^4$ electrons are collected, inducing a charge of $4 \cdot 10^{-15}$ Coulomb on the readout strip.

The total signal produced by an energetic electron or photon is calculated similarly. About 12 % of the total shower energy appears as ionization in the liquid argon gaps, the rest being dissipated in the lead planes. Assuming complete containment of a 1 GeV shower, the 120 MeV of ionization energy released in the liquid argon produces $4.6 \cdot 10^6$ ion pairs, leading to an induced charge of about $0.4 \cdot 10^{-12}$ Coulomb.

2.5.4 Calibration

The electronics of the LA system was calibrated daily during normal data taking by means of the calibration system sketched in figure 6(b). An external calibration pulser applied pulses of known voltage to a 10 pf capacitor coupled to each channel of the electronics. The risetime of the applied pulses was matched to the charge drift time (600 ns) in the 3 mm liquid argon gaps. The output signal was processed like real data, and an offset, gain, and rms noise value were calculated for each channel. Corrections were made for the capacitance of the detector strips (plus high voltage blocking capacitor), which diverted some of the injected charge away from the preamplifiers.

During real data taking, the stored calibration constants were used to determine a minimum pulseheight cut (channel offset plus one standard deviation of noise) for signals to be recorded and to convert the measured signals into equivalent liquid argon ionization energies. The calibrations were also used to flag dead or very noisy channels for repair. During normal operation, the failure rate was only a few channels (out of 3000) per week.

2.5.5 Energy Resolution

The intrinsic energy resolution of the LA system for electromagnetic showers was governed by the sampling nature of the calorimeters. An average of 12 % of the total incident energy of an electron or photon was deposited as ionization on the liquid argon gaps. The dominant factor affecting the resolution was just the fluctuations in this fraction of the total energy sampled by the calorimeter.

A simple calculation of this fluctuation, based on an estimate of the number of independent samplings of deposited energy, can be used to estimate the expected resolution of the LA calorimeters. An ionizing particle passing through a single liquid argon cell deposits 1.3 MeV of ionization energy in the liquid argon, or about 10 MeV in the combined lead plus liquid argon. Treating each passage of one ionizing particle through one cell as an independent energy measurement, an incident particle of total energy E will yield (E/10 MeV) such measurements. Statistical fluctuations in this number (neglecting correlations among the ionizing particles of the shower) lead to an expected energy resolution given by $\sigma/E \approx 10\% / \sqrt{E}$ (E in GeV).

The actual energy resolution of the LA system was measured to be $\sigma/E = 12\% / \sqrt{E}$ (E in GeV) over a wide range of electron energies. Figure 7 shows the measured LA energy for electrons from Bhabha scattering events taken at a beam energy of 1.55 GeV. The width of the LA energy distribution in this plot (FWHM $\leq$ 400 MeV) corresponds to an energy resolution of $\sigma \simeq 11\% \sqrt{E}$. The distribution is slightly non-Gaussian due to radiative effects.

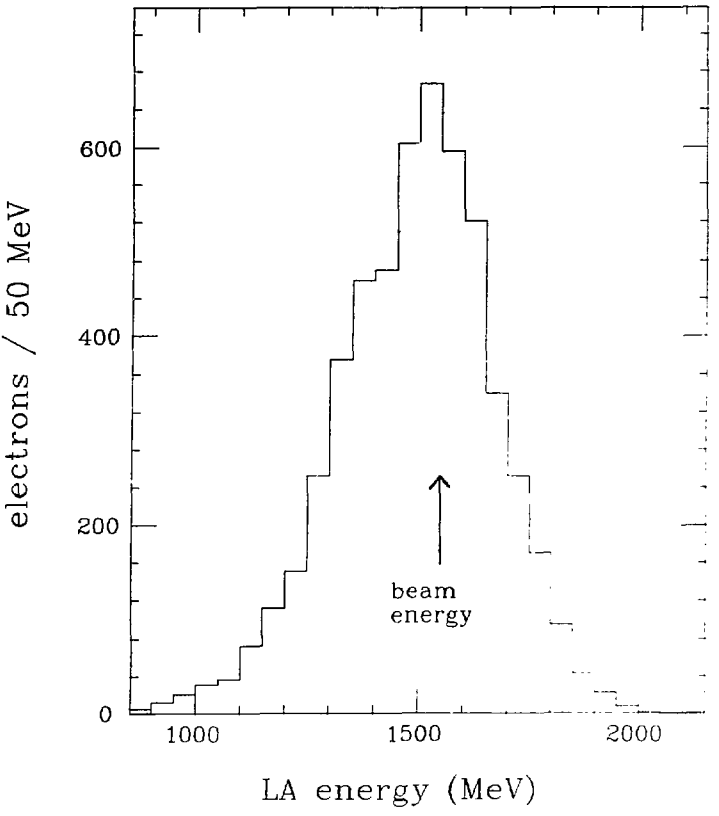

Figure 7: LA energy resolution for electrons

1.55 Gev Bhabha electrons (E_{cm} = 3.1 GeV)

2.6 PION - ELECTRON SEPARATION BY LA

One of the primary functions of the LA system was to identify electrons. In order to separate electrons from the much larger number of pions produced in hadronic events, good use must be made of the properties of electromagnetic showers in the LA calorimeters. The LA calorimeter sandwich used high Z material (lead) in order to maximize its thickness for electromagnetic interactions (14 radiation lengths) while minimizing its thickness for hadronic interactions (0.5 absorption lengths), thus emphasizing the differences between electromagnetic and hadronic showers. The most important differences between electromagnetic showers and the tracks of minimum ionizing or interacting hadrons are the following :

1) total energy deposition

Electromagnetic showers release nearly the full energy of an incident electron within a LA calorimeter, so that the measured LA energy of an electron is roughly equal to its momentum. Minimum ionizing hadrons deposit ionization equivalent to an electron of about 200 MeV in their passage through a LA calorimeter. Interacting hadrons deposit several times this energy. At high momenta total LA energy measurements can be used to provide good pion - electron separation without any additional information from the LA system.

2) longitudinal energy deposition

Electromagnetic showers begin in the first few radiation lengths of a LA calorimeter and develop rapidly, dissipating most of the en-

ergy of an incident electron within the front half of the calorimeter. Minimum ionizing hadrons deposit ionization energy uniformly along their paths through a LA calorimeter. Interacting hadrons initiate hadronic showers in the LA calorimeter, but hadronic showers develop much more slowly (in depth) than do electromagnetic showers, due to the small thickness of the lead - liquid argon stack in absorption lengths compared to its thickness in radiation lengths. Longitudinal measurements of shower development are particularly important for pion - electron separation at low energies.

3) transverse energy deposition

Electromagnetic showers are generally contained within a small transverse region about the projected track of an incident electron. The same is true for minimum ionizing hadrons. Interacting hadrons can scatter at relatively large angles, generating broader showers, but even in this case the transverse width information is of only marginal use in the separation of pions from electrons. An additional problem was that the typical transverse spread of a shower in the LA calorimeters was comparable to the readout strip width of a few cm. The width of a shower which deposited energy on only one or two strips could not be accurately determined.

LA separation of real pions and electrons is illustrated in figure 8, a scatterplot of LA energy vs momentum. Tracks plotted in figure 8(a) were electrons taken from reconstructed photon conversions in the beam pipe. A clear band of tracks with LA energy equal to the track momentum can be seen. Tracks plotted in figure 8(b) were pions taken from reconstructed ψ decays ($\psi \rightarrow 2\pi^+2\pi^-\pi^0$). A clear band of minimum

ionizing tracks can be seen, along with a number of interacting pions which deposited substantially more energy in the liquid argon.

The actual pion - electron separation was performed by a program (LAESEP) written by Jonathan Dorfan [13] . This program uses a method known as 'recursive partitioning for nonparametric classification' to construct a binary tree of decisions (cuts) used to separate different classes of events. The decisions are based on measured quantities (separation variables) whose distributions for the classes of events to be separated are not known. The cuts are chosen to optimize the separation of sets of events (training vectors) whose classification is known.

For separation of pions and electrons, the sets of training vectors were samples of known pions and electrons, identified without the use of LA information. Pions were taken from ψ decays of the form $\psi \rightarrow 2\pi^+2\pi^-\pi^0$, identified by requiring the mass recoiling against the four observed charged particles to be consistent with a missing neutral pion ($m < 630$ MeV/c^2). Contamination of the pion sample by electrons from photon conversion was reduced to the 2-3 % level by eliminating events containing two oppositely charged tracks with a small opening angle ($\cos\theta > .99$). Electrons with momentum greater than 700 MeV/c were taken from radiative Bhabha scattering events, identified by requiring the track opposite the electron candidate to have momentum close to the beam momentum ($.85 < p/E_b < 1.08$) and LA energy consistent with the beam energy ($.58 < E_{LA}/E_b < 1.2$). Pion contamination of the radiative Bhabha electrons was negligible. Electrons with momentum less than 700 MeV/c were taken from photon conversions, identified by reconstructing a secondary vertex at the pipe counter radius and requiring the opening

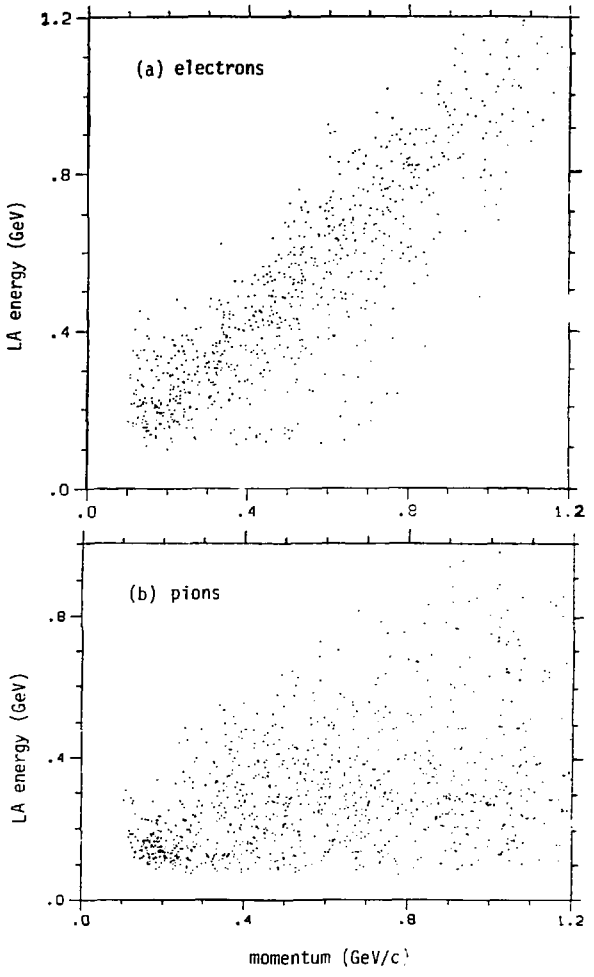

Figure 8: LA energy deposition by electrons and pions

(a) LA energy vs momentum for electrons from photon conversions
(b) LA energy vs momentum for pions from reconstructed τ decays

angle between the two tracks to be small ($\cos\theta > .99$). Pion contamination of the photon conversion electrons was estimated at 2 % .

The separation variables used to discriminate pions from electrons were derived primarily from LA measurements, supplemented with information from the DC and TOF systems. Several variables related to the theory of electromagnetic shower development were specifically included. The complete list of separation variables was the following :

- track momentum (p)
- TOF electron weight (for p < 500 MeV/c)
- angle of incidence of track to LA module
- χ^2 of match between LA shower location and DC projected track position
- total energy deposited in LA divided by track momentum (E_{LA}/p)
- energy deposited in each LA layer ($E_{TR}, E_{F1}, E_{F2}, E_{F3}, E_{T1}, E_{T2}, E_U$)
- transverse width of pulseheight distribution in each LA layer ($\sigma_{TR}, \sigma_{F1}, \sigma_{F2}, \sigma_{F3}, \sigma_{T1}, \sigma_{T2}, \sigma_U$)
- energy deposited in front half of LA module divided by track momentum ($(2E_{TR}+E_{F1}+E_{F2}+E_{T1}+E_U) / p$)
- depth (X) of maximum energy deopsition in LA ($X = \Sigma E_i X_i / \Sigma E_i$, where X_i = average depth of layer i)
- longitudinal spread (δX) of energy deposition in LA ($\delta X^2 = \Sigma(X-X_i)^2 E_i / \Sigma E_i$)
- an empirically found quantity $E_{F1} \cdot (E_{T1}+E_U)/p$

Decision trees were constructed to classify unknown particles on the basis of these separation variables. Cuts leading to good discrimination between pions and electrons were chosen by examining the values of the separation variables for the previously selected samples of known pions and electrons. The separation program used these cuts to classi-

fy unknown particles, assigning an unknown particle to a particular classification bin according to the values of its separation variables. The final identification of the unknown particle was then made on the basis of the numbers of known pions and electrons which fell into the same classification bin. For the analysis in later chapters, a particle was called an electron if more than 90 % of the known particles in its classification bin were real electrons.

3. INCLUSIVE BARYON PRODUCTION

The Mark II collaboration has previously published measurements of the cross sections for proton and lambda production as functions of center-of-mass energy at SPEAR [14] . These measurements are reported again here because they are important to a quantitative understanding of charmed baryon production in e^+e^- annihilation. Estimates of the fraction of proton and lambda events which are due to charmed baryon production and decay and estimates of the charmed baryon production cross section derived here will be used in the next two chapters to determine the branching ratios of various charmed baryon decays.

Most of the analysis presented here was done by Jeff Weiss and has not been repeated for this thesis. Only brief details of the analysis will be given before moving on to the results and conclusions.

Antiprotons were identified by time-of-flight in events with two or more detected charged tracks. Protons were not used because of the large background of events with stray protons produced by beam-gas interactions. The TOF weighting technique described in the preceding chapter was used to separate antiprotons from pions and kaons. A TOF weight cut of 0.5 was used for antiprotons with momentum less than 1.2 GeV/c ; at higher momenta (up to 2.0 GeV/c) the stricter TOF weight cut of 0.7 was used. A correction was made for contamination of the antiproton sample by misidentified pions and kaons (less than 15 %).

Lambdas and antilambdas were identified from the invariant mass distribution of $p\pi^-$ and $\bar{p}\pi^+$ pairs of tracks (with protons and antiprotons identified by time-of-flight as above) in events with three or more de-

tected charged tracks. The decay particles were required to originate from a reconstructed secondary vertex. To reduce the beam-gas proton background, lambda events (but not antilambda events) were required to have total observed charge less than or equal to zero. Corrections were made for the remaining combinatorial background under the lambda and antilambda mass peaks (less than 15 %).

The most difficult part of this analysis was the determination of the overall efficiency for identifying protons and lambdas, which in turn depends on the momentum spectra of the produced protons and lambdas. A Monte Carlo model of baryon production was used to generate events with an antiproton or lambda momentum distribution given by the invariant cross section $d\sigma/dp \propto (p^2/E) \exp(-bE)$ [15]. The slope parameter b was adjusted to give a good fit to the antiproton data at each center-of-mass energy. Additional pions (and one nucleon) were generated according to the remaining phase space, with mean charged particle multiplicity adjusted to match the antiproton data at each center-of-mass energy. The Monte Carlo calculation included initial state radiation, DC and TOF efficiencies, and TOF resolution . Corrections for nuclear absorption of protons and lambdas were also made. The overall antiproton and lambda detection efficiencies were then calculated from the Monte Carlo generated events.

The model of the antiproton and lambda spectra is needed to extrapolate the observed spectrum to low momenta, where the detection efficiency falls to zero. The model indicates that roughly 15 % of the antiproton momentum spectrum falls below 300 MeV/c and roughly 40 % of the lambda momentum spectrum falls below 500 MeV/c, where the detection efficiencies are essentially zero. The overall antiproton detection

efficiency is approximately 60 % at all energies and the overall lambda detection efficiency ranges from 12 % at 3.67 GeV to 15 % at 7.4 GeV.

The calculated cross sections for inclusive production of protons and lambdas (normalized to the QED cross section for muon pair production) are presented in table 4 and plotted in figure 9. The values of R_Λ presented here are 20 % lower than the previously published values, which were calculated using an incorrect value for the Λ^0 detection efficiency (caused by an error in the Monte Carlo program). Statistical errors are shown. Systematic errors, estimated at 17 % for antiprotons and 27 % for lambdas, are not included. These systematic errors are dominated by the model dependence of the Monte Carlo calculation and are expected to vary slowly with center-of-mass energy.

Protons from lambda decay are included in the inclusive proton cross section R_p and lambdas from sigma decay are included in the inclusive lambda cross section R_Λ.

Clear increases in R_p and R_Λ are observed in the 4.5 - 5.2 GeV center-of-mass energy range, possibly continuing at higher energies. It is natural to associate the observed threshold in R_p and R_Λ at 4.5 GeV with the onset of charmed baryon production. The observed increase in R_p can then be used to determine the charmed baryon production cross section.

Several assumptions are necessary to calculate an absolute cross section from the measurments of R_p --

1) The observed step in R_p is assumed to be due entirely to charmed baryon pair production. (Associated production of a charmed baryon and a charmed meson ($\Lambda_c\bar{D}^0\bar{p}$ or $\Lambda_c D^-\bar{n}$) has not been seen; the cross section for associated production is less than 0.4 nb at 5.2 GeV [16].)

TABLE 4

Inclusive proton and lambda production

Ecm (GeV)	$R_p + R_{\bar{p}}$	$R_\Lambda + R_{\bar{\Lambda}}$
3.52	.390 ± .035	.046 ± .020
3.67	.371 ± .014	.058 ± .009
3.77	.388 ± .009	.066 ± .007
4.02	.351 ± .016	.039 ± .010
4.16	.354 ± .012	.064 ± .009
4.27	.356 ± .016	.070 ± .014
4.43	.398 ± .015	.068 ± .011
4.55	.434 ± .030	.066 ± .018
4.65	.444 ± .030	.133 ± .027
4.75	.471 ± .032	.085 ± .024
4.84	.536 ± .031	.094 ± .019
4.95	.539 ± .031	.113 ± .024
5.04	.534 ± .034	.139 ± .028
5.14	.678 ± .038	.163 ± .030
5.21	.674 ± .011	.130 ± .009
5.58	.686 ± .043	.160 ± .047
5.87	.742 ± .077	.125 ± .054
6.57	.790 ± .021	.205 ± .015
7.40	.960 ± .210	.176 ± .034

$R_p = \sigma(e^+e^- \to pX) / \sigma(e^+e^- \to \mu^+\mu^-)$
$R_\Lambda = \sigma(e^+e^- \to \Lambda X) / \sigma(e^+e^- \to \mu^+\mu^-)$

$R_p + R_{\bar{p}}$ is actually calculated as $2R_{\bar{p}}$ since only antiprotons are used in the analysis.

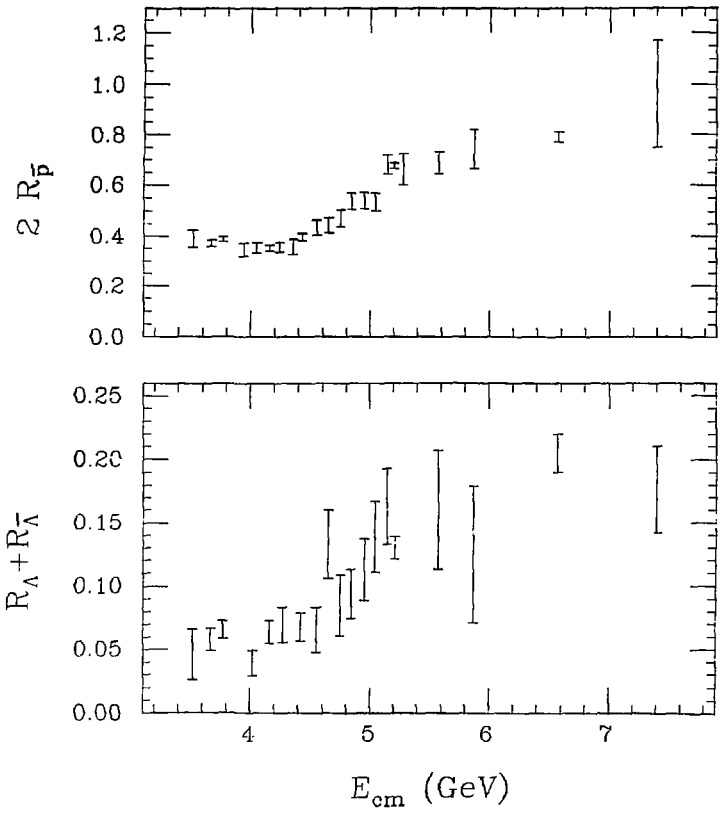

Figure 9: Inclusive proton and lambda production

(a) $R_p = \sigma(e^+e^- \to pX) / \sigma(e^+e^- \to \mu^+\mu^-)$ vs E_{cm}
(b) $R_\Lambda = \sigma(e^+e^- \to \Lambda X) / \sigma(e^+e^- \to \mu^+\mu^-)$ vs E_{cm}

2) All higher mass charmed baryons are assumed to decay strongly down to the Λ_c state. Weak decays of charmed baryons other than the Λ_c are neglected.

3) The Λ_c is assumed to decay to a proton (rather than a neutron) with probability $F_p = (0.6 \pm 0.1)$. (There are more open channels for Λ_c decay to proton final states than there are to neutron final states. The value $F_p = 0.6$ is an estimate based on a statistical model of hadronic Λ_c decays [17].)

The first assumption is the most critical. If only part of the observed rise in R_p is due to charmed baryon production, the calculated charmed baryon production cross section will be an overestimate of the actual cross section. With these assumptions, the charmed baryon production cross section is calculated as

$$\sigma(\Lambda_c) + \sigma(\bar{\Lambda}_c) = [\Delta R_p + \Delta R_{\bar{p}}]\ (F_p)^{-1}\ \sigma(\mu\mu)$$

where $\sigma(\Lambda_c) = \sigma(e^+e^- \to \Lambda_c\ X)$
$\sigma(\mu\mu) = \sigma(e^+e^- \to \mu^+\mu^-)$
$\Delta R_p = R_p(E_{cm}) - R_p(\text{below } 4.5 \text{ GeV})$

Putting in the observed step size $\left(\Delta R_p + \Delta R_{\bar{p}}\right) = (0.31 \pm 0.06)$ at $E_{cm} = 5.2$ GeV gives the final result

$$\sigma(\Lambda_c) + \sigma(\bar{\Lambda}_c) = (1.7 \pm 0.4)\ \text{nb} \qquad \text{at } E_{cm} = 5.2 \text{ GeV}.$$

4. HADRONIC DECAYS OF THE CHARMED BARYON

The Mark II collaboration has previously presented results on the observation of hadronic decays of the lowest lying charmed baryon Λ_c [18] . The decays $\Lambda_c^+ \to pK^-\pi^+$ and $\Lambda_c^+ \to pK_S^0$ (and their charge conjugates $\bar{\Lambda}_c^- \to \bar{p}K^+\pi^-$ and $\bar{\Lambda}_c^- \to \bar{p}K_S^0$) have been observed as peaks in invariant mass spectra. From these observed decays, the mass of the Λ_c has been determined to be $m(\Lambda_c) = (2285 \pm 6)$ MeV/c^2.

At the fixed center of mass energy of 5.2 GeV, the cross section times branching ratio for the $pK\pi$ decay mode has been measured to be $[\ \sigma(\Lambda_c) + \sigma(\bar{\Lambda}_c)\ ] \cdot BR\ (\Lambda_c^+ \to pK^-\pi^+) = (\ 0.037 \pm 0.012)$ nb.

Using Mark II measurements of the inclusive proton cross section as a function of center-of-mass energy to independently determine the total charmed baryon cross section, the $\Lambda_c \to pK\pi$ branching ratio has been estimated to be $BR\ (\Lambda_c^+ \to pK^-\pi^+) = (2.2 \pm 1.0)$ % .

In this chapter, these results will be presented again in somewhat more detail. Some aspects of the present analysis differ significantly from the previous analysis, but the final numbers are all in quite good agreement (well within the estimated systematic and statistical errors). The different values presented here can be taken as an indication of how much variation is to be expected from the use of different analysis techniques; they are not meant to replace the previously published values.

4.1 DATA SAMPLE

The data sample used in this analysis represents an integrated luminosity of 13700 nb^{-1}, taken at center of mass energies from 4.5 to 6.8 GeV. Runs at 5.2 GeV account for about 5800 nb^{-1} of this luminosity.

Events selected for analysis were required to have a reconstructed primary vertex (common intersection point of good charged tracks) near the known beam crossing point. The actual cuts on the location of the primary vertex were $|Z_v| < 7.5$ cm (Z_v is the longitudinal distance from the interaction point to the primary vertex, measured along the beam direction) and $R_v < 1.5$ cm (R_v is the radial distance from the interaction point to the primary vertex, measured in the plane perpendicular to the beam direction). Plots of these vertex distributions for events containing an identified proton and an identified kaon are shown in figure 10. The cuts are chosen to result in only a small loss of good events (estimated at less than 4 %), while removing a fair number of background events. Beam-gas interactions, in particular, have a very broad Z distribution; they are responsible for most of the events in the tails of the Z_v plot.

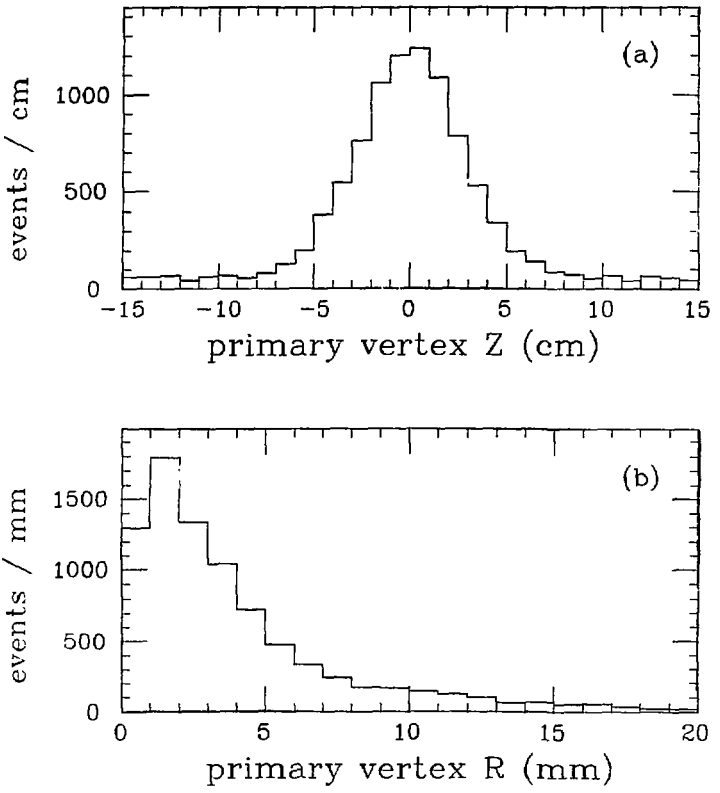

Figure 10: Vertex distributions for proton - kaon events

(a) vertex distribution along beam axis (Z_V)
(b) vertex distribution in plane perpendicular to beam axis (R_V)

4.2 $\Lambda_c \rightarrow pK\pi$ DECAY MODE

The decay $\Lambda_c^+ \rightarrow pK^-\pi^+$ (plus $\bar{\Lambda}_c^- \rightarrow \bar{p}K^+\pi^-$) provides the most prominent charmed baryon signal observed in the Mark II detector.

Protons, kaons, and pions were identified by time-of-flight, using the weighting technique described in chapter 2. For this analysis, the criteria used to identify these particles were as follows :

- protons : TOF proton weight > 0.5
  momentum < 2.0 GeV/c
- kaons : TOF kaon weight > 0.5
  momentum < 1.4 GeV/c
- pions : TOF mass squared < 0.3 $(GeV/c^2)^2$
  not identified as a proton or a kaon

Tracks with no TOF information were assumed to be pions. Tracks identified as muons by the muon system and tracks identified as electrons by the liquid argon and TOF systems were eliminated.

In addition, each track was required to originate at the primary vertex of the event. Two loose cuts were made on the calculated distance of closest approach of each track to the primary vertex —

1) The longitudinal distance of closest approach (along the beam axis) was required to be less than 6 cm.
2) The radial distance of closest approach (in the xy plane perpendicular to the beam axis) was subjected to the momentum dependent cut $R_{min} \cdot P_\perp$ < 8 mm GeV/c. ($P_\perp = P_{xy}$ is the momentum in the plane perpendicular to the beam axis.)

The momentum dependence of the second cut is designed to offset the effect of small angle multiple Coulomb scattering, which results in a

measurement error inversely proportional to the momentum of the particle. The inefficiency introduced by these two cuts is less than 2 % per track.

The $pK\pi$ invariant mass was calculated using the beam constrained momenta of the proton, kaon, and pion (which reduces the momentum error by requiring the tracks to originate at the known beam interaction point). Corrections were made for dE/dx energy losses, amounting to several MeV per track, in the material preceding the drift chamber.

Figure 11(a) shows the $pK\pi$ invariant mass distribution for the 'charmed' channel $pK^-\pi^+$ (plus $\bar{p}K^+\pi^-$) expected from the weak decay of a charmed baryon (or antibaryon). A requirement that the mass recoiling against the $pK\pi$ system be greater than 2200 MeV/c^2 has been applied. (In e^+e^- annihilation, the lowest mass charmed baryon must be produced in association with states of equal or greater mass.) A definite peak is observed at a mass of 2286 MeV/c^2, with a Gaussian width of 16 MeV/c^2. The peak contains (55 ± 11) events above a combinatorial background of 14 events per 10 MeV/c^2 bin.

Figure 11(b) shows the same $pK\pi$ invariant mass distribution with the requirement that the recoil mass be less than 2200 MeV/c^2. No signal is evident, demonstrating that the observed $pK\pi$ state is indeed being produced in association with states of equal or greater recoil mass.

Invariant mass distributions for the 'uncharmed' channels $pK^+\pi^-$ (plus $\bar{p}K^-\pi^+$) and $pK^-\pi^-$ (plus $\bar{p}K^+\pi^+$) exhibit no structure, demonstrating that the observed $pK\pi$ state is the decay mode of a charmed baryon.

The efficiency for detecting the $pK\pi$ decay mode of the charmed baryon was determined by a Monte Carlo calculation. The Mark II Monte Carlo program HOWL was used to generate 14000 charmed baryon decays of the

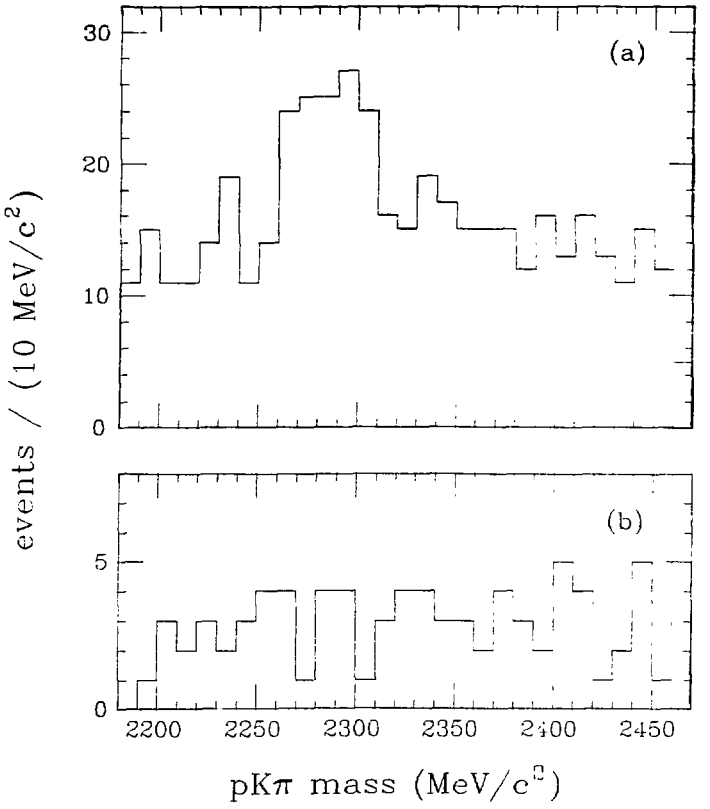

Figure 11: pKπ invariant mass distributions

(a) $pK^-\pi^+$ ($\bar{p}K^+\pi^-$) mass for states with recoil mass > 2200 MeV/c^2
(b) $pK^-\pi^+$ ($\bar{p}K^+\pi^-$) mass for states with recoil mass < 2200 MeV/c^2

form $\bar{\Lambda}_c^-(2285) \rightarrow \bar{p}K^+\pi^-$, using initial $\bar{\Lambda}_c$ momenta ranging from 0 to 2100 MeV/c. The Monte Carlo program generated raw data (drift times for hits in each DC layer, flight times for hits in TOF counters, etc.) for each particle traversing the detector. Losses due to nuclear interactions and errors due to energy loss and multiple Coulomb scattering in the material preceding the drift chamber were taken into account. Kaons were allowed to decay in flight. A drift chamber resolution of 200 μ and a time-of-flight resolution of 300 ps were used. The raw data generated by the Monte Carlo were then passed through the same tracking and particle identification programs used to analyze the real data.

The efficiency for reconstructing the decay $\Lambda_c \rightarrow pK\pi$ was determined, as a function of Λ_c momentum, by plotting the $pK\pi$ invariant mass spectra for various Λ_c momentum ranges and performing Gaussian fits to determine the numbers of $pK\pi$ events in the Λ_c mass peaks. Figure 12 gives the resulting $\Lambda_c \rightarrow pK\pi$ detection efficiency as a function of Λ_c momentum. The efficiency is nearly momentum independent and has an average value of (15 ± 2) %. The quoted error includes statistical as well as systematic uncertainties in the accuracy with which the Monte Carlo program simulates real data.

The Monte Carlo generated invariant mass plots also predict the width of the $pK\pi$ state expected from the limited drift chamber resolution. The Gaussian width of the Monte Carlo generated $pK\pi$ peak is independent of the Λ_c momentum and has an average value of (13 ± 2) MeV/c^2.

From the observed number of $\Lambda_c \rightarrow pK\pi$ decays, the $pK\pi$ detection efficiency, and the luminosity of the data sample, the product of the Λ_c

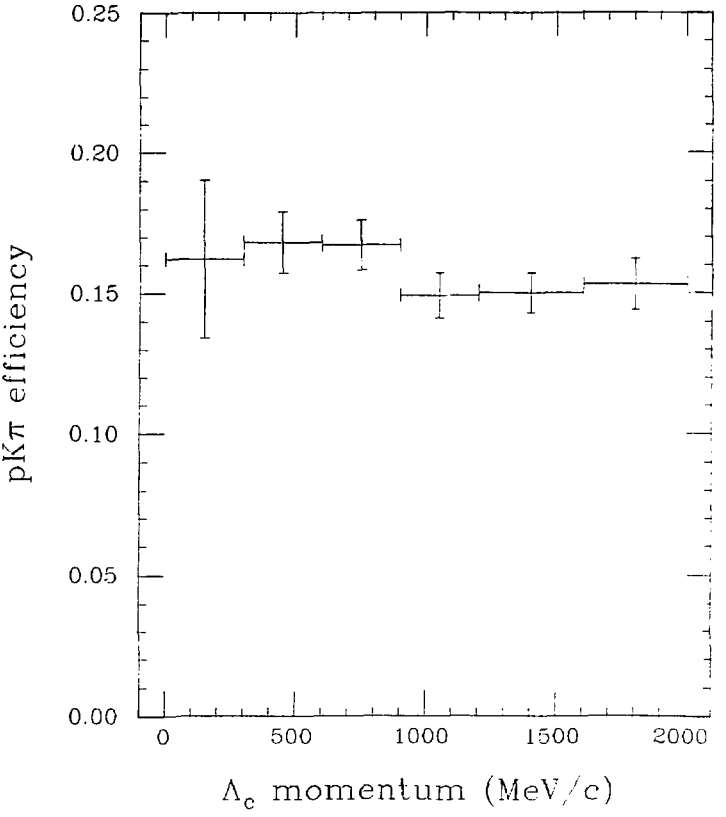

Figure 12: $\Lambda_c \to pK\pi$ detection efficiency

production cross section and the $\Lambda_c \to pK\pi$ branching ratio can be calculated. For this purpose, the large block of data collected at the fixed center-of-mass energy 5.2 GeV was used. In this data, the $pK\pi$ peak contains (29 ± 8) events from a luminosity of 5790 nb^{-1}, giving

$$[\ \sigma(\Lambda_c) + \sigma(\bar{\Lambda}_c)\ ] \cdot BR\ (\Lambda_c^+ \to pK^-\pi^+) = (.034 \pm .010)\ nb.$$

In the last chapter, the absolute charmed baryon production cross section at 5.2 GeV was estimated to be $[\ \sigma(\Lambda_c) + \sigma(\bar{\Lambda}_c)\ ] = (1.7 \pm 0.4)$ nb. This determines the $\Lambda_c \to pK\pi$ branching ratio separately as

$$BR\ (\Lambda_c^+ \to pK^-\pi^+) = (2.0 \pm 0.8)\ \%\ .$$

4.3 $\Lambda_c \to pK^0_S$ DECAY MODE

The decay $\Lambda_c \to pK^0_S$ (plus $\bar{\Lambda}_c \to \bar{p}K^0_S$) has also been definitely observed in the Mark II detector. Protons were identified by time-of-flight using the same criteria as for the $pK\pi$ decay. Neutral kaons were identified by reconstructing the decay $K^0_S \to \pi^+\pi^-$. A secondary vertex finding program (written by Rafe Schindler) was used to perform this reconstruction in the following steps :

1) Collect $\pi^+\pi^-$ pairs of tracks.

2) Find radial crossing point (R_V) of tracks. Require 2 mm $< R_V <$ 30 cm (note $c\tau \simeq 2.7$ cm for K^0_S).

3) Find Z coordinates of tracks at crossing point. Require $\frac{1}{2}|Z_1+Z_2| <$ 30 cm and $|Z_1-Z_2| <$ 8 cm.

4) Recalculate proton and pion momenta and directions at vee position (including dE/dx corrections).

5) Calculate direction of vector from the interaction point to the vee and direction of $p\pi$ momentum at the vee, both in the x-y plane. Require these two directions to agree to within 60°.

6) Calculate invariant mass of the vee.

7) Perform a 1C fit to the K^0 mass, keeping vees with reasonable fits. This is roughly equivalent to requiring the $\pi^+\pi^-$ invariant mass to be within about 15 MeV/c^2 of the K^0 mass.

The $\pi^+\pi^-$ invariant mass spectrum after cuts 1-5 is plotted in figure 13 for events containing an identified proton. The combinatorial background is about half as large as the K^0_S signal.

Figure 14(a) shows the observed pK^0_S invariant mass distribution, again with the requirement that the mass recoiling against the pK^0_S system be greater than 2200 MeV/c^2. An enhancement is observed at the same mass as in the $pK\pi$ channel, consisting of (17 ± 6) events above a combinatorial background of 2.4 events per 10 MeV/c^2 bin. The pK^0_S in-

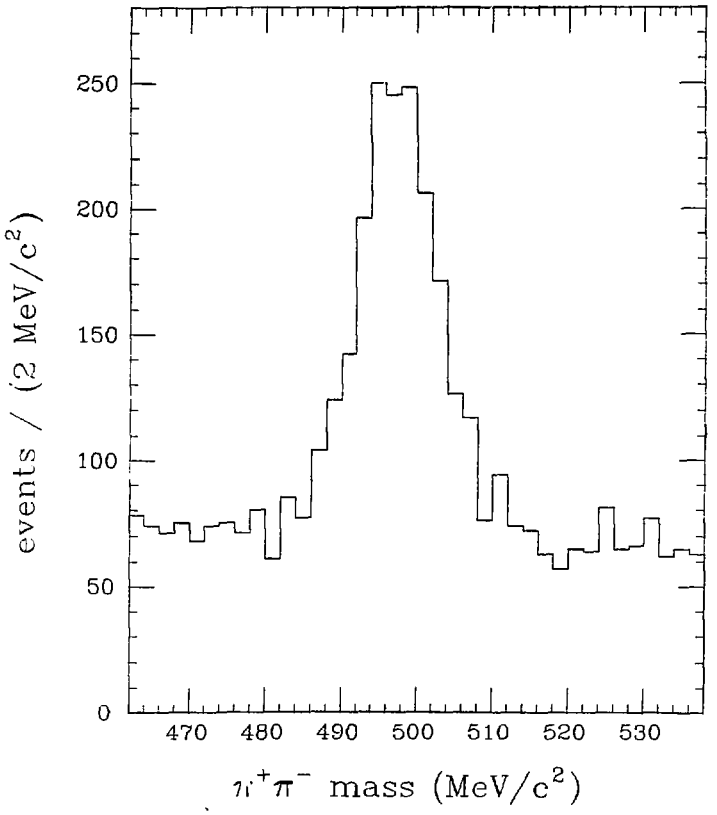

Figure 13: $\pi^+\pi^-$ invariant mass spectrum in proton events

variant mass distribution for recoil masses less than 2200 MeV/c^2, plotted in figure 14(b), shows no structure. In the 5.2 GeV data alone, similar plots yield a Λ_c signal of (11 ± 4) events above background.

The efficiency for detecting the pK^0_S decay mode of the charmed baryon was determined by a Monte Carlo calculation similar to that used for the $pK\pi$ decay mode. K^0_S particles were generated and allowed to decay within the Mark II detector according to the standard branching ratios (68.6 % to $\pi^+\pi^-$) and lifetime ($c\tau$ = 2.675 cm). K^0_S particles were reconstructed from their $\pi^+\pi^-$ decays with the same program used for the real data.

Figure 15 gives the resulting $\Lambda_c \to pK^0_S$ detection efficiency (including the $K^0_S \to \pi^+\pi^-$ branching ratio) as a function of Λ_c momentum. The efficiency is not quite flat, falling slowly with increasing Λ_c momentum. The overall pK^0_S efficiency is (13 ± 2) % , averaged over the Λ_c momentum spectrum observed in the $pK\pi$ channel. The width of the pK_S invariant mass peak predicted by the Monte Carlo is again independent of the Λ_c momentum and has an average value of (16 ± 2) MeV/c^2.

From the number of observed $\Lambda_c \to pK\pi$ and $\Lambda_c \to pK^0_S$ decays and the relative detection efficiencies for the two decay modes, the $\Lambda_c \to pK^0_S$ branching ratio can be determined relative to the $\Lambda_c \to pK\pi$ branching ratio as

$$\frac{BR\ (\Lambda_c^+ \to pK^0_S)}{BR\ (\Lambda_c^+ \to pK^-\pi^+)} = \frac{(17 \pm 6)\ (.15 \pm .02)}{(55 \pm 11)\ (.13 \pm .02)} = (36 \pm 16)\ \%$$

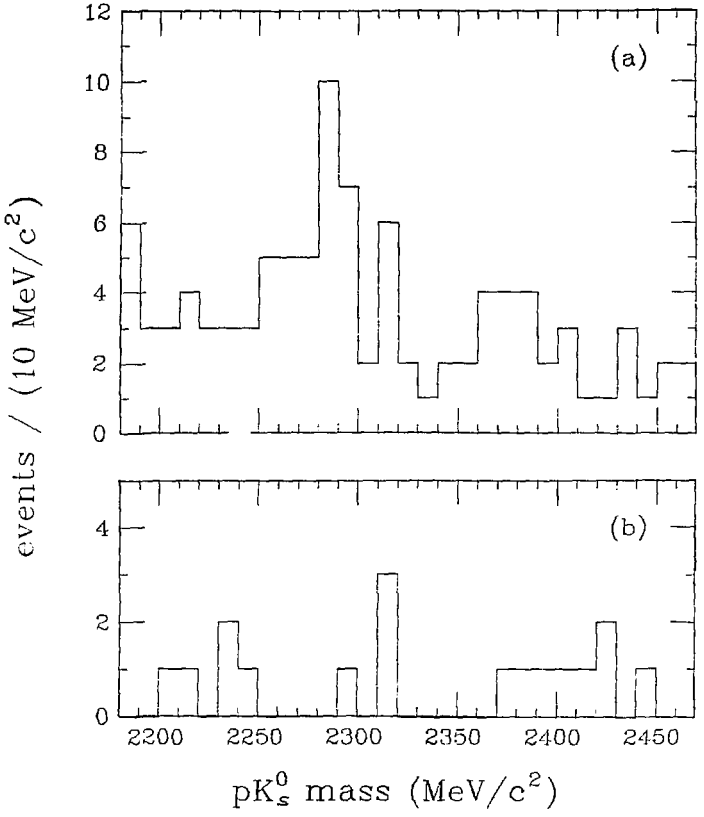

Figure 14: pK^0_s invariant mass distributions

(a) pK^0_s ($\bar{p}K^0_s$) mass for states with recoil mass > 2200 MeV/c^2
(b) pK^0_s ($\bar{p}K^0_s$) mass for states with recoil mass < 2200 MeV/c^2

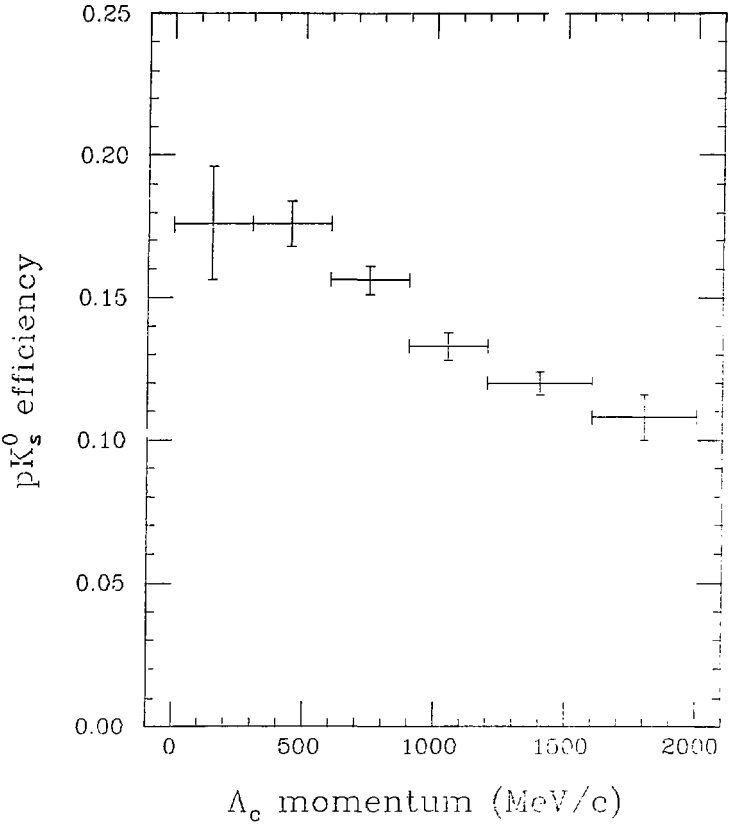

Figure 15: $\Lambda_c \to pK^0_s$ detection efficiency

4.4 $\Lambda_c \to \Lambda^0\pi$ DECAY MODE

The decay $\Lambda_c^+ \to \Lambda^0\pi^+$ (plus $\bar{\Lambda}_c^- \to \bar{\Lambda}^0\pi^-$) has not been observed in the Mark II detector.

Lambdas were identified by a secondary vertex finding program very similar to that used to find neutral kaons. The various cuts used for finding lambdas and plots of the resulting lambda mass are discussed fully in the next chapter.

Figure 16(a) gives the observed $\Lambda^0\pi$ invariant mass distribution for the 'charmed' channel $\Lambda^0\pi^+$ (plus $\bar{\Lambda}^0\pi^-$), again with the requirement that the mass recoiling against the $\Lambda^0\pi$ system be greater than 2200 MeV/c^2. No enhancement is observed near 2285 MeV/c^2. From the level of the combinatorial background and the number of events in the Λ_c signal region, an upper limit of 6 (90 % confidence level) can be set on the number of $\Lambda_c \to \Lambda^0\pi$ decays which might be present.

The efficiency for detecting the $\Lambda^0\pi$ decay mode of the charmed baryon was again determined by a Monte Carlo calculation similar to that used for the $pK\pi$ and pK^0_S decay modes. Lambdas were generated and allowed to decay within the Mark II detector using the standard branching ratios (64.2 % to $p\pi$) and lifetime ($c\tau$ = 7.89 cm). These lambdas were then reconstructed from their $p\pi$ decays using the same program used for the real data.

Figure 17 gives the resulting $\Lambda_c \to \Lambda^0\pi$ detection efficiency as a function of Λ_c momentum. The efficiency is nearly independent of the Λ_c momentum and has an average value of (8.5 ± 2) %. The Gaussian width of the $\Lambda^0\pi$ invariant mass peak predicted by the Monte Carlo is (17 ± 2) MeV/c^2.

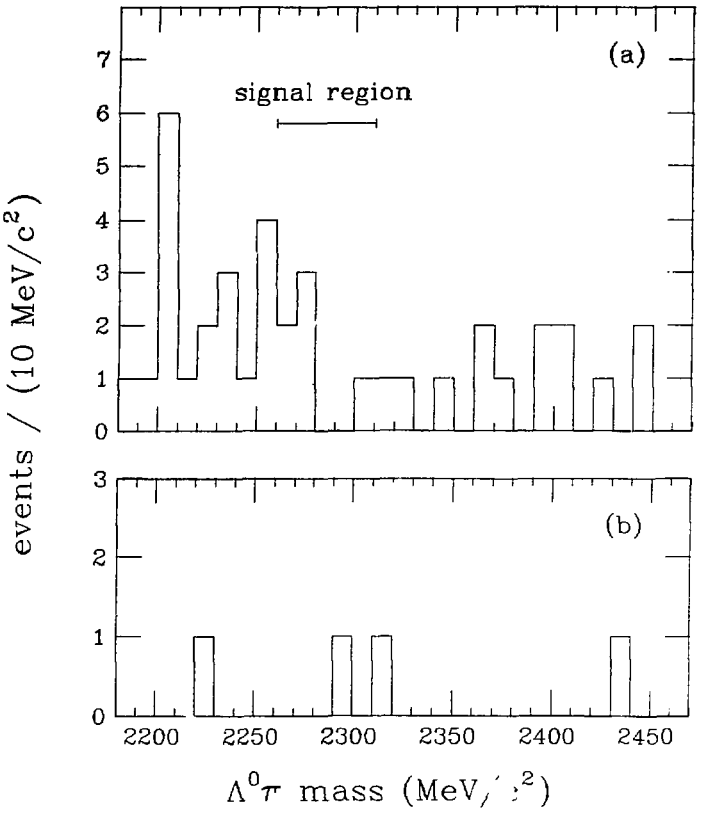

Figure 16: $\Lambda^0\pi$ invariant mass distribution (recoil mass > 2200 MeV/c^2)

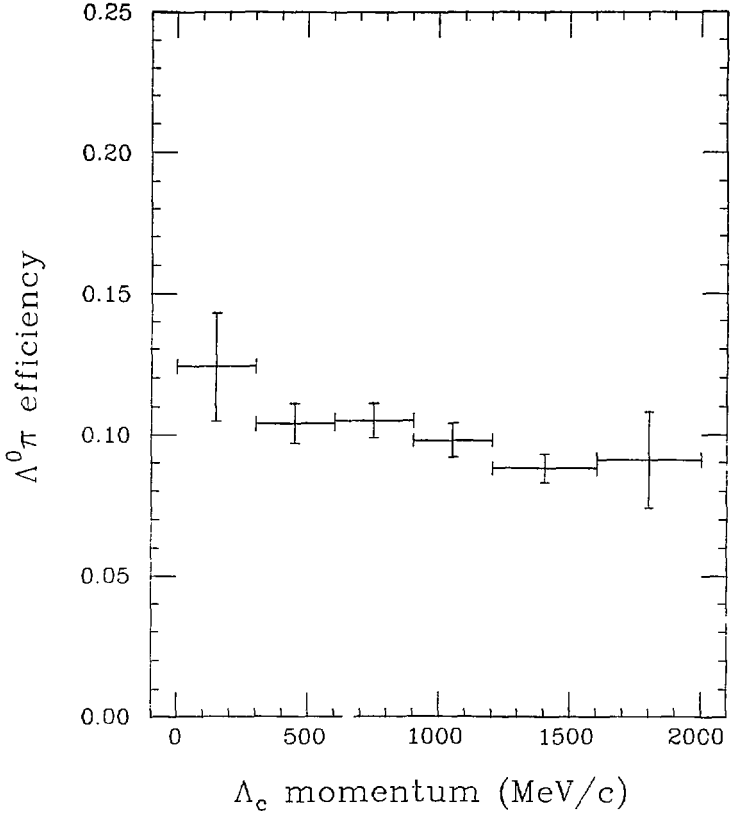

Figure 17: $\Lambda_c \to \Lambda^0\pi$ detection efficiency

The upper limit on the possible number of $\Lambda_c \to \Lambda^0\pi$ decays, the number of observed $\Lambda_c \to pK\pi$ decays, and the relative efficiencies for the two decay modes imply a branching ratio limit of

$$\frac{BR\ (\Lambda_c^+ \to \Lambda^0\pi^+)}{BR\ (\Lambda_c^+ \to pK^-\pi^+)} < \frac{(6)\ (.15 \pm .02)}{(55 \pm 11)\ (.085 \pm .02)} < 25\ \% \qquad (90\%\ \text{cl.})$$

This limit is more stringent tham the previously published Mark II limit of 80 % , which was based on beam constrained mass plots with more limited statistics.

4.5 Λ_c MASS DETERMINATION

Figure 18 gives the Λ_c mass distribution for the combined $pK\pi$ and pK^0 channels. Included in the figure is a fit to a Gaussian peak on top of a flat background. The fit gives a Λ_c mass value of $m(\Lambda_c) = (2286 \pm 4)$ MeV/c^2.

The largest systematic error in the Λ_c mass determination comes from the uncertainty in the value of the magnetic field which is used to calculate the momenta of charged particles. During data taking, the magnetic field is continuously monitored by an NMR probe, determining the field strength to an accuracy of 0.2 % . Changing the value of the magnetic field used in the tracking programs by this amount changes the calculated value of the Λ_c mass by 4 MeV/c^2.

A smaller systematic error could be caused by the dE/dx correction applied to all charged tracks to correct for energy loss in the material preceding the drift chamber. Omitting the dE/dx correction entirely changes the calculated value of the Λ_c mass by 10 MeV/c^2. The dE/dx correction itself should be good to the 10 % level, leading to an error of 1 MeV/c^2 in the Λ_c mass from this source.

Adding the systematic errors in quadrature with the statistical error from the fit gives an overall error of 6 MeV/c^2 in the determination of the Λ_c mass.

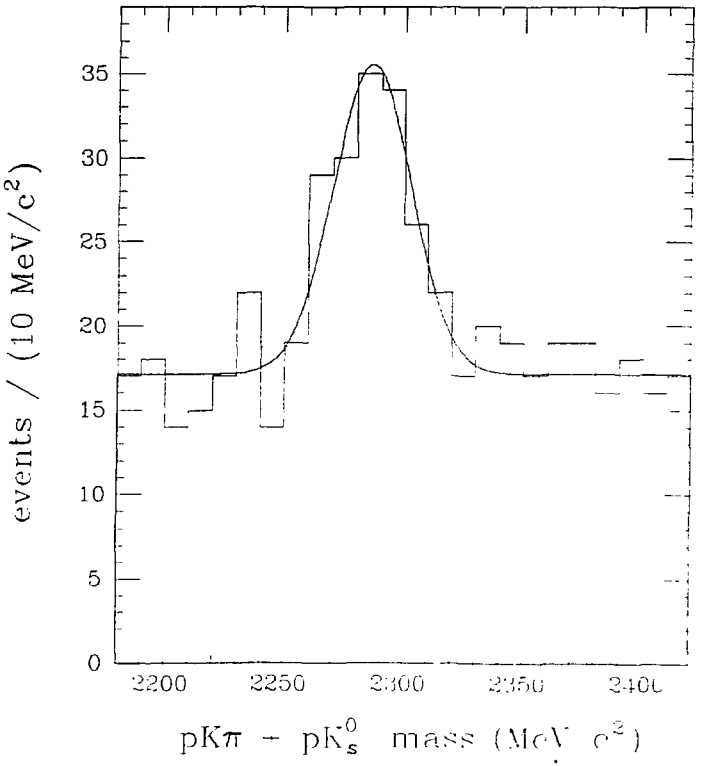

Figure 18: $pK\pi$ plus pK^0_s invariant mass distribution (recoil mass > 2200 MeV/c^2)

4.6 HIGHER MASS CHARMED BARYONS

4.6.1 Λ_c Recoil Mass

The invariant mass of the system recoiling against the observed $pK\pi$ and pK^0_S states is plotted in figure 19. All $pK\pi$ and pK^0_S states with invariant masses falling within 25 MeV/c^2 of the Λ_c mass (2285 MeV/c^2) contribute to figure 19 (a) . The shape of the background is indicated in figure 19 (b), which uses $pK\pi$ and pK^0_S states with invariant masses falling in sidebands extending from 35 to 135 MeV/c^2 away from the Λ_c mass on either side.

Two body production of the Λ_c , $e^+e^- \rightarrow \Lambda_c\bar{\Lambda}_c$, is responsible for the excess of events with recoil mass near the Λ_c mass. These events can be seen in a more unbiased way by looking at the invariant mass distribution of all states having equal recoil mass. Figure 20 is an invariant mass plot of all $pK\pi$ and pK^0_S states whose recoil mass is within 50 MeV/c^2 of their observed mass. There are (12 ± 4) events peaked near the Λ_c mass, above a background of 0.4 events per 10 MeV/c^2 bin. The Λ_c peak in the 5.2 GeV data alone consists of (6.5 ± 2.7) events above background. Compared with the (40 ± 10) $pK\pi$ and pK^0_S events with recoil mass greater than 2200 MeV/c^2 in the Λ_c peak at 5.2 GeV, this implies that the reaction $e^+e^- \rightarrow \Lambda_c\bar{\Lambda}_c$ is responsible for (16 ± 8) % of the total Λ_c production at 5.2 GeV.

Two body production of higher mass charmed baryons, $e^+e^- \rightarrow \Sigma_c\bar{\Sigma}_c$ or $(\Sigma^*_c\bar{\Sigma}_c + \Sigma_c\bar{\Sigma}^*_c)$ or $\Sigma^*_c\bar{\Sigma}^*_c$, followed by the decay $\Sigma_c \rightarrow \Lambda_c\pi$ or $\Sigma^*_c \rightarrow \Lambda_c\pi$,

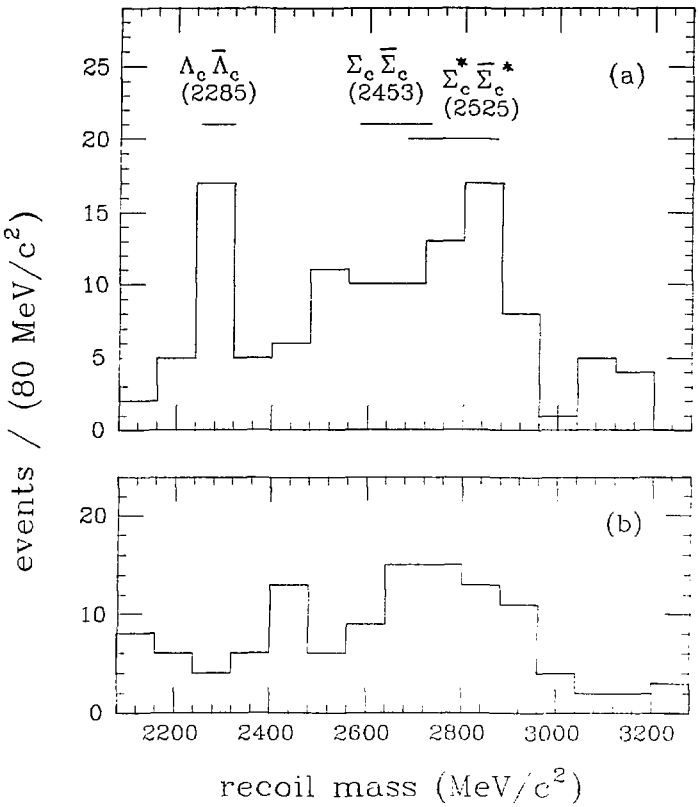

Figure 19: pKπ plus pK^0_S recoil mass distributions

(a) Λ_c signal region -- (2285 ± 25) MeV/c^2
(b) background region -- (2320-2420) MeV/c^2 and (2150-2250) MeV/c^2

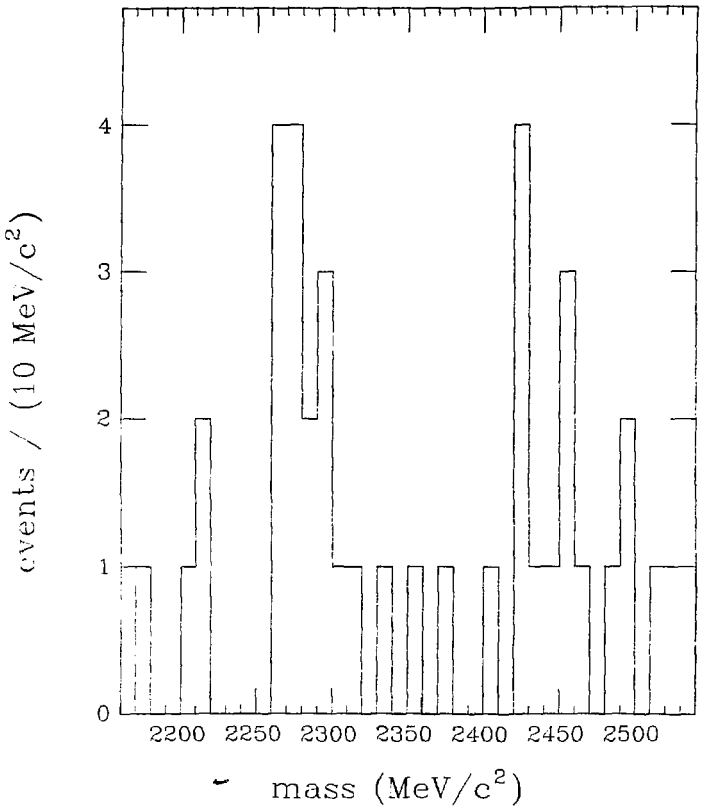

Figure 20: Equal recoil invariant mass distribution

$pK\pi$ plus pK^0_S mass distribution for states with recoil mass within 50 MeV/c² of observed mass

would show up in figure 19 as an excess of events with recoil masses 200-300 MeV/c^2 higher than the Σ_c or Σ_c^* mass and spread over a range of about ±100 MeV/c^2 (due to the momentum of the extra pion included with the Σ_c or Σ_c^* in the system recoiling against the observed Λ_c). The expected location of these peaks has been indicated in figure 19 for charmed baryons with masses of 2450 MeV/c^2 and 2525 MeV/c^2. Clearly neither of these production processes is dominant, but they may well contribute at some level.

Multibody production of charmed baryons and mesons, such as $e^+e^- \rightarrow \Lambda_c\bar{\Lambda}_c\pi\pi$, would give rise to a very broad recoil mass distribution, starting several humdred MeV/c^2 above the Λ_c mass and extending to the kinematic limit $E_{cm} - m(\Lambda_c)$. This production process may well also be present.

4.6.2 Σ_c Reconstruction

Higher mass charmed baryons have been searched for more directly by attempting to reconstruct the cascade decay $\Sigma_c \rightarrow \Lambda_c\pi$ and plotting the mass difference $\Delta m = m(\Sigma_c) - m(\Lambda_c)$. Many systematic errors cancel in the calculation of the mass difference, making it a more useful quantity than the directly calculated Σ_c mass.

Good efficiency for low momentum tracks is necessary to detect the pion produced in this decay. For a mass difference of 168 MeV/c^2, for example, the cascade pion would have a momentum of about 90 MeV/c in the rest frame of the Σ_c ; at 5.2 GeV center-of-mass energy, the boost into the lab frame would spread this momentum over a range of ±60 MeV/c.

Since the standard Mark II drift chamber tracking program has very poor efficiency for tracks with momentum less than 100 MeV/c, a modified program was written (by Heidi Schellman) to track lower momentum particles. This program recovers most "loopers" (tracks which are too highly curved to reach the outermost drift chamber layers) and extends the drift chamber tracking limit down to about 60 MeV/c.

A Monte Carlo calculation was performed to determine the efficiency of reconstructing the decay $\Sigma_c \to \Lambda_c\pi$ with this modified tracking program. 9000 cascade decays $\Sigma_c \to \Lambda_c\pi$ ($\Lambda_c \to pK\pi$) were generated, using a mass difference $\Delta m = 168$ MeV/c^2. Raw data from these Monte Carlo events were analyzed with the same programs used for the real data, including the modified drift chamber tracking program. In those events in which the Λ_c was well reconstructed, the additional pion (if tracked) was used to calculate the Σ_c mass. A plot of the mass difference produces a very narrow peak, centered at the correct value, with a Gaussian width of 4 MeV/c^2. The efficiency for reconstructing the decay $\Sigma_c \to \Lambda_c\pi$, given a reconstructed Λ_c, is 40 % for this mass difference. Larger mass differences result in higher efficiencies, up to the geometric limit of 75 % for a mass difference of 240 MeV/c^2.

The same procedure was used to search for higher mass charmed baryons in the real data. $pK\pi$ and pK^0_S states in the Λ_c mass peak (2285 ± 25 MeV/c^2) were combined with any extra pions in the event, and a new invariant mass was calculated. The mass of the system recoiling against the $\Lambda_c\pi$ state was required to be greater than 2400 MeV/c^2. The mass difference $\Delta m = m(\Lambda_c\pi) - m(\Lambda_c)$ is plotted in figure 21. No clear indication of a cascade decay can be seen, demonstrating at least that cascade decays are not the dominant Λ_c production mechanism. Given the

limited statistics, however, no strong statement about the level of Σ_c production can be made. If 5 of the 8 events in the 160-170 MeV/c^2 bins were attributed to the Σ_c, for example, this would imply that the cascade decay $\Sigma_c \rightarrow \Lambda_c\pi$ was responsible for 25 % of the total Λ_c production.

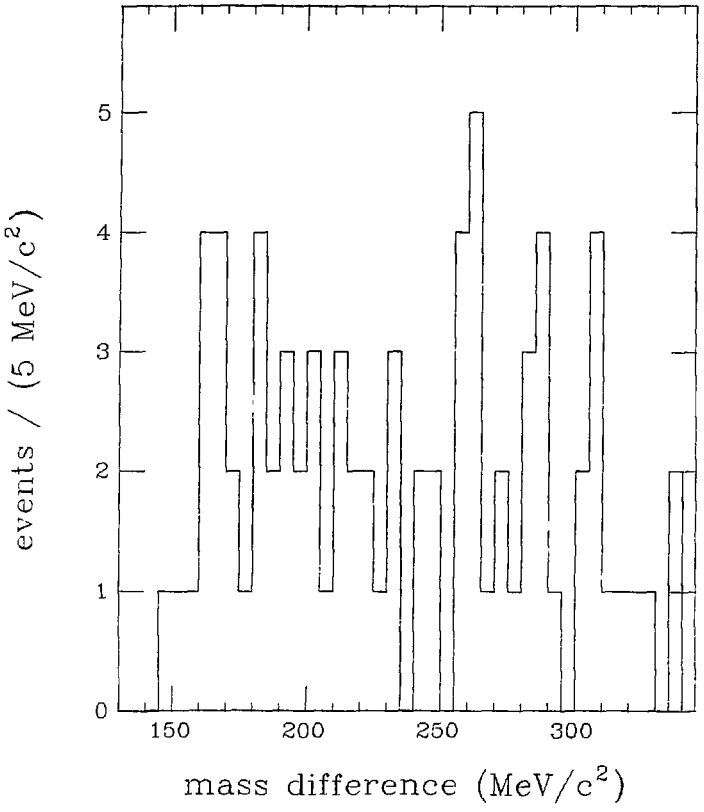

Figure 21: Σ_c - Λ_c mass difference

$m(pK\pi\pi) - m(pK\pi)$ for $m(pK\pi) = 2265 \pm 25$ MeV/c²
$m(pK^0\pi) - m(pK^0_S)$ for $m(pK^0_S) = 2285 \pm 25$ MeV/c²

5. SEMILEPTONIC DECAYS OF THE CHARMED BARYON

This analysis attempts to identify prompt electrons produced in the semileptonic decays of charmed baryons. Events containing antiprotons, lambdas, or antilambdas are used as event samples with a large charmed baryon content. Electrons are identified using a combination of time of flight and liquid argon information. Subtractions are made for electrons produced by sources other than charm and for pions misidentified as electrons. The remaining electron signal, corrected for detection efficiency, is used to calculate the fraction of baryon events containing an electron. Together with an estimate of the fraction of the baryon event sample resulting from charmed baryon production and decay, this gives a measurement of the semileptonic branching ratio of the charmed baryon.

5.1 DATA SAMPLE

Essentially all of the SPEAR data with center of mass energy from 4.5 to 6.8 GeV were used in this analysis. Additional data taken at lower energy (below the threshold for charmed baryon pair production) were used as a check. There should be no direct electron signal in this lower energy data (primarily ψ' events) because there is no mechanism for producing both a baryon and an electron in the same event (apart from small sources like semileptonic decays of kaons) below the charmed baryon threshold. The data were divided into several E_{cm} ranges to look for threshold effects.

Two separate baryon event samples were used :

1) events with an antiproton

2) events with a lambda or an antilambda

The antiproton event sample included antiprotons from antilambda decays. Events with a proton but no antiproton were not used because of the large background of protons produced by beam - gas interactions.

Table 5 gives a breakdown of the different baryon event samples by center of mass energy. The procedure by which the different baryon events were selected is discussed in the following sections.

TABLE 5

Baryon event samples

E_{cm} (GeV)	$\int Ldt$ (nb^{-1})	N_p	$N_{\bar{\Lambda}}$	$N_{\Lambda}^{\dagger}$
3.68	800	8271	735	728
3.77	2070	704	40	56
3.8 - 4.5	3240	1017	51	57
	---	---	---	---
	4310	9992	826	841
4.5 - 5.1	2690	944	84	62
5.1 - 5.3	5790	2358	188	181
5.3 - 6.2	1440	545	51	37
6.2 - 6.8	3800	1362	113	121
	---	---	---	---
	13720	5209	436	401

† Lambda events passing charge cut, with background ≈ 20 % of sample

5.1.1 Baryon Identification

Antiprotons were identified by time-of-flight, using the weighting technique described in chapter 2. In order to be identified as an antiproton, a particle was required to pass the following cuts :

- Track origin at the primary vertex (or at a reconstructed antilambda vertex);
- Momentum less than 2.0 GeV/c ;
- TOF proton weight greater than 0.7 .

The antiproton sample is quite free of contamination by misidentified pions and kaons. Figure 22 is a scatterplot of momentum vs. mass

squared for all negatively charged tracks with mass squared greater than 0.15 $(GeV/c^2)^2$ in data taken at 5.2 GeV. The solid curve marks the boundary between kaons and protons corresponding to a TOF proton weight of 0.7. Bands of protons and kaons begin to merge at momenta greater than 1 GeV/c, but there are relatively few tracks in this momentum range. The overall contamination of the antiproton sample by misidentified pions and kaons is estimated at 5 % .

Lambdas and antilambdas were identified by reconstructing the decays $\Lambda^0 \rightarrow p\pi^-$ and $\bar{\Lambda}^0 \rightarrow \bar{p}\pi^+$. A secondary vertex finding program (written by Rafe Schindler) performed the reconstruction in the following steps :

1) Collect $p\pi^-$ and $\bar{p}\pi^+$ pairs of tracks. Here protons are defined by the somewhat looser time-of-flight cuts :

   proton weight > 0.40 for momentum < 1.2 GeV/c
   proton weight > 0.65 for momentum > 1.2 GeV/c .

2) Find radial crossing point (R_v) of tracks. Require $0 < R_v < 30$ cm (note $c\tau \simeq 8$ cm for Λ^0).

3) Find Z coordinates of tracks at crossing point. Require $\frac{1}{2}|Z_1+Z_2| < 30$ cm. and $|Z_1-Z_2| < 20$ cm.

4) Recalculate proton and pion momenta and directions at vee position (including dE/dx corrections).

5) Calculate direction of vector from the interaction point to the vee and direction of $p\pi$ momentum at the vee, both in the xy plane. Require these two directions to agree to within 60^0.

6) Calculate invariant mass of the vee.

7) Perform a 1C fit to the lambda mass, keeping vees with reasonable fits. This is roughly equivalent to requiring the proton - pion invariant mass to be within about 6 MeV/c^2 of the lambda mass.

The $p\pi$ invariant mass spectra after cuts 1-5 are plotted in figure 23 for both antilambdas and lambdas. Antilambdas are almost completely background free, but there is a large combinatorial background under the lambda peak, arising from stray protons produced by beam - gas in-

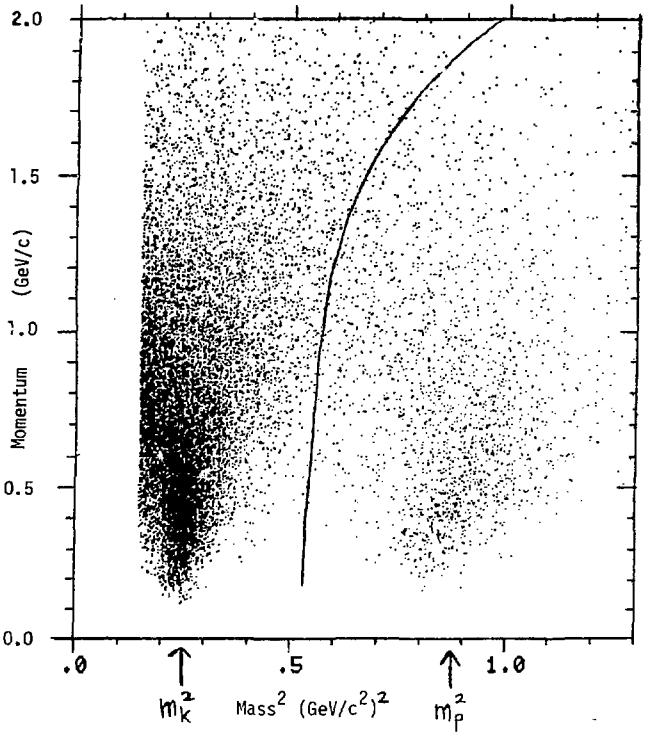

Figure 22: Proton identification by TOF

negatively charged tracks from events at 5.2 GeV
solid curve marks boundary at TOF proton weight = 0.7

teractions. This background can be reduced considerably by imposing several requirements on the event as a whole (not just the proton and the pion forming the lambda) designed to discriminate against beam - gas events, as described in the next section.

The efficiencies for finding the various baryon events do not enter into any of the calculations of the electron signals or semileptonic branching ratios in the rest of this analysis, but they are presented here for completeness. Proton and lambda detection efficiencies were determined by a Monte Carlo calculation using 41000 generated tracks of each type with momenta ranging from 0 to 2000 MeV/c. Lambdas were allowed to decay into protons and pions with the correct lifetime ($c\tau$ = 7.89 cm) and branching ratio (64.2 % to $p\pi$). The detected tracks were passed through the same proton and lambda finding programs used in the real data analysis. Figure [illegible] plots the resulting detection efficiencies.

The proton detection efficiency is about 60-70 % for momenta from 400 to 1400 MeV/c. At lower momenta the efficiency falls rapidly (to 0 at 300 MeV/c) as slow protons range out in the material preceding the drift chamber; at higher momenta the efficiency falls slowly (to 30 % at 2000 MeV/c) as the proton weight cut becomes increasingly important. The lambda detection efficiency is about 18-21 % (including the $p\pi$ branching ratio) for momenta from 700 to 1700 MeV/c. At lower momenta the efficiency falls rapidly (to 0 at 400 MeV/c); at higher momenta the efficiency falls slowly (to 13 % at 2000 MeV/c).

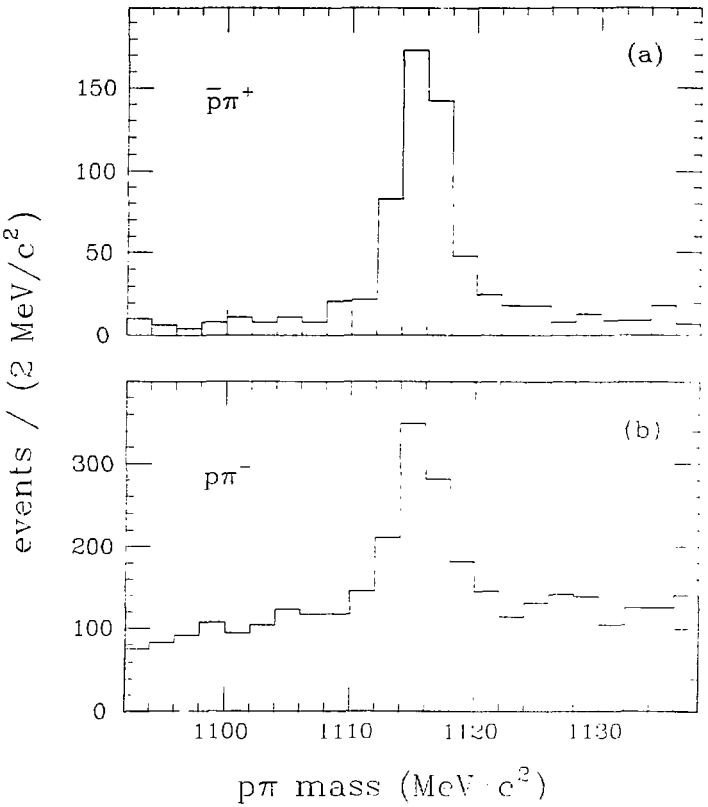

Figure 23: $\bar{p}\pi^+$ and $p\pi^-$ invariant mass spectra

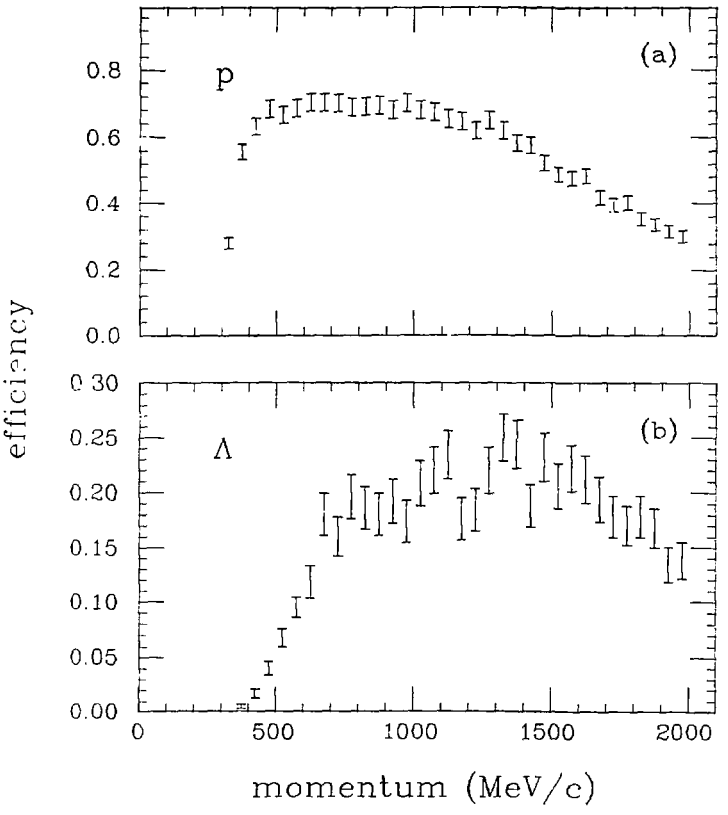

Figure 24: Proton and lambda detection efficiencies

5.1.2 Event Selection

Events used in this analysis were required to have three or more charged particles. A reconstructed primary vertex, near the known beam crossing point, was also required. (Decay products of lambdas were required to originate at a reconstructed secondary vertex and were therefore excluded from the primary vertex.) The actual cuts on the location of the primary vertex were

1) longitudinal distance from vertex to interaction point (projected along the beam axis) : $|Z_v| < 9$ cm.

2) radial distance from vertex to interaction point (projected in xy plane perpendicular to beam axis) : $R_v < 2$ cm.

The Z_v cut, in particular, is useful for eliminating events caused by beam - gas interactions. Z_v distributions for antiproton, antilambda, and lambda events are shown in figure 25 . Note the long tail of lambda events with large $|Z_v|$. Both the Z_v and R_v cuts are loose enough to result in a negligible loss of beam - beam interaction events.

To further reduce the background in lambda events, a cut was made on the total charge of all tracks in the event. Lambda events with positive charge were eliminated, unless they also contained an identified antiproton to mark the event as good. Since beam - gas events with a stray proton have higher average charge than do good events, this cut is able to substantially reduce the level of beam - gas background without causing too large a loss of good events. This effect is illustrated in figure 26, which shows $p\pi^-$ invariant mass distributions for lambda events passing and failing the total charge cut. In these plots

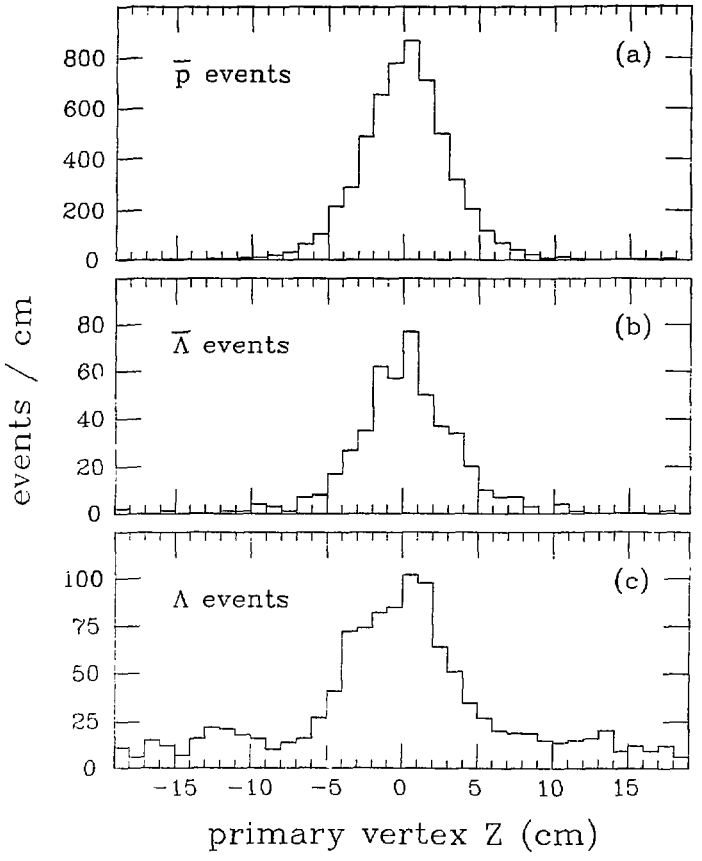

Figure 25: Primary vertex Z_v distributions

(a) antiproton events (b) antilambda events (c) lambda events

the Z_v cut has not yet been applied, so the full beam - gas background is still present and the effect of the charge cut is maximized. From a comparison of the effects of the charge cut on lambda events (signal plus beam - gas background) with the effects of the opposite charge cut on antilambda events (signal with essentially no beam - gas background), the charge cut is found to remove 70-75 % of the background lambda events and 20-25 % of the real lambda events. The remaining lambda events (with net charge zero or less) contain an estimated background of 20 % and were used in the analysis.

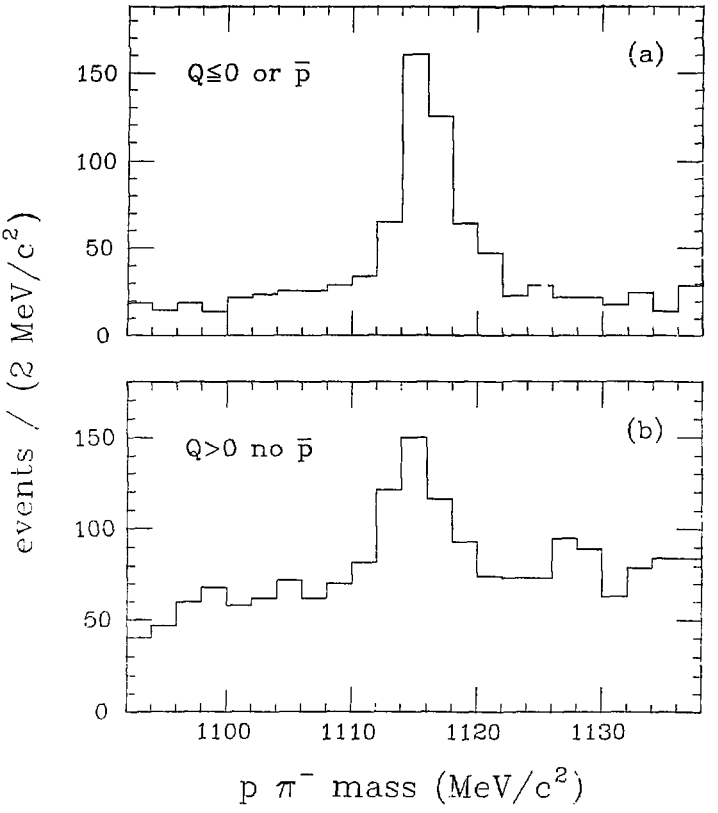

Figure 26: $p\pi^-$ invariant mass spectra with charge cut

(a) events passing charge cut ($Q \leq 0$) or containing an antiproton
(b) events failing charge cut ($Q > 0$) and not containing an antiproton

5.2 CALCULATION OF ELECTRON SIGNAL

The basic quantity calculated in this analysis is the number of prompt electrons produced in baryon events. This calculation is performed in the following stages:

1) Collect candidate electrons and pions satisfying certain quality criteria.

2) Separate electrons from pions as well as possible.

3) Remove electrons obviously arising from photon conversions.

4) Subtract background of pions misidentified as electrons.

5) Subtract remaining background of secondary electrons.

6) Correct for electron detection efficiency.

The philosophy followed in this procedure has been to identify real electrons as cleanly as possible, even at the cost of some reduction in efficiency.

5.2.1 Electron Identification Procedure

All electron candidates were required to pass two cuts on the distance of closest approach of the track to the e^+e^- interaction point. These cuts are designed to insure that the tracks originate at the primary vertex.

1) The longitudinal distance of closest approach (along the beam axis) was required to be less than 7.5 cm. The efficiency of this cut for good tracks is 98 % .
2) The radial distance of closest approach (in the xy plane perpendicular to the beam axis) was subjected to the momentum dependent cut $R_{min} \cdot P_\perp < 5$ mm GeV/c. ($P_\perp = P_{xy}$ is the particle momentum in the plane perpendicular to the beam axis.) The efficiency of this cut for good tracks is over 99 % .

The momentum dependence of the second cut is designed to offset the effect of small angle multiple Coulomb scattering, which results in a measurement error inversely proportional to the momentum of the particle. An added advantage of this particular cut is that it removes most electrons produced by photon conversions in the 3 mm thick (.009 radiation length) Lexan window surrounding the drift chamber at a radius of 37 cm. A simple calculation shows that the tracks of an electron pair produced at this radius project back to a distance of closest approach to the interaction point satisfying $R_{min} \cdot P_\perp \approx 8$-9 mm GeV/c. Unfortunately, the more numerous photon conversions which occur in the vacuum chamber pipe (.012 radiation length) at 8 cm radius and in the pipe counter assembly (.038 radiation length) at 12 cm radius project back

to $R_{min} \cdot P_{\perp} < 1$ mm GeV/c and cannot be eliminated with this technique. To become an electron candidate, a track of any momentum was required to have a good time-of-flight measurement (99 % efficiency within the 75 % of 4π solid angle coverage of the time-of-flight system). The time-of-flight requirement for tracks with momenta less than 300 MeV/c was somewhat stricter — double hits and tracks which hit far from their projected position along the length of the scintilator were eliminated (87 % efficiency). Finally, the measured time-of-flight was required to agree with the time-of-flight expected for an electron to within the loose cut of 1.2 ns (about four standard deviations). To become an electron candidate, a track with momentum greater than 300 MeV/c was required to also have a good liquid argon measurement. Tracks hitting a liquid argon module too close to an edge were eliminated (88 % efficiency within the 64 % of 4π solid angle coverage of the liquid argon system).

The final electron identification procedure depended on the momentum of the electron candidate. Electrons with momentum less than 300 MeV/c were identified by TOF alone. LA measurements were used in conjunction with TOF measurements to separate pions from electrons at momenta greater than 300 MeV/c. Above 500 MeV/c, electron identification relied solely on LA information.

To identify candidate electrons with momentum less than 300 MeV/c, the TOF weighting technique described in chapter 2 was used. Pion and electron TOF weights were calculated, and tracks with electron weight greater than 0.9 were identified as electrons. This relatively high weight cut was chosen to insure a low probability of misidentifying a pion as an electron (since real pions far outnumber real electrons in the data).

Figure 27 contains scatterplots of $(t-t_\pi)$ vs. $(t-t_e)$ for 2900 low momentum pions and electrons taken from antiproton events with $E_{cm} > 4.5$ GeV. t is the measured time-of-flight and t_π and t_e are the calculated times-of-flight for pions and electrons respectively. In these coordinates, tracks of a fixed momentum populate a thin line, concentrated at $(t-t_e) = 0$ for electrons and $(t-t_\pi) = 0$ for pions. The assumed boundary between pions and electrons at electron weight = 0.9 is a hyperbola which intersects this line (see figure 27). The plots are divided into several momentum ranges to show the changing pion - electron separation ability of the TOF system.

The electron identification above 300 MeV/c was performed by the program LAESEP described in chapter 2. This program uses samples of known pions and electrons to construct a binary tree of cuts which are then used to classify unknown particles. For this analysis, a particle was called an electron if more than 90 % of the known particles falling into the same final classification bin were real electrons. Again, the relatively high cut was chosen to reduce the probability of misidentifying a pion as an electron, at the expense of some efficiency in identifying electrons.

Because so many separation variables are used, it is difficult to visualize the actual electron identification process as a whole. The most important separation variable for high momentum particles is the total energy deposited in a LA calorimeter. Figure 28 is a scatterplot of total LA energy vs. momentum for 8800 tracks taken from antiproton events with $E_{cm} > 4.5$ GeV. A band of minimum ionizing pions is evident at all momenta. A smaller band of interacting pions, which deposit a significant fraction of their energy in the LA calorimeter, can also be

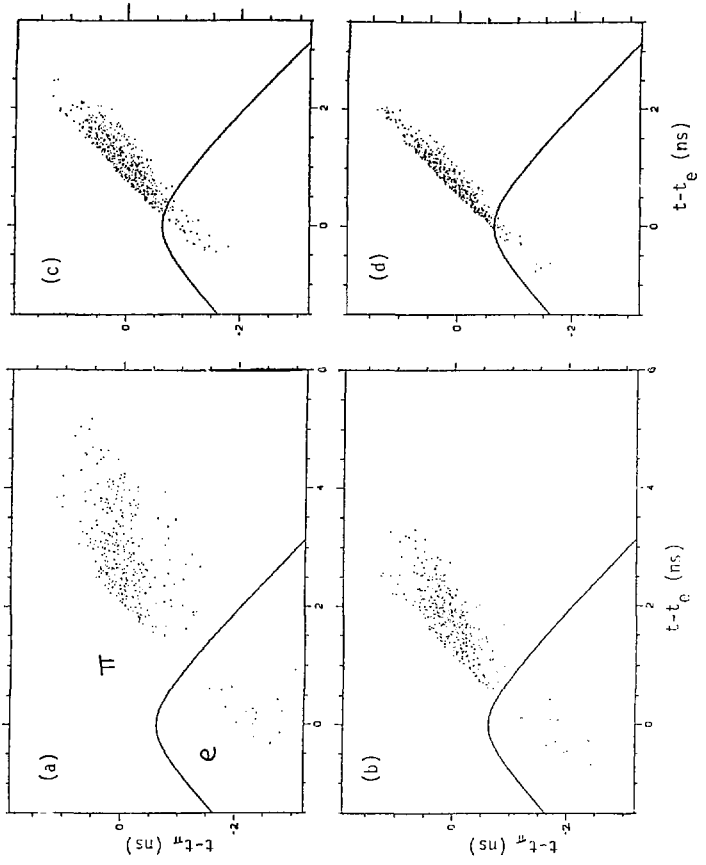

Figure 27: $(t-t_\pi)$ vs. $(t-t_e)$ for pions and electrons

(a) 100 MeV/c < p < 150 MeV/c (b) 150 MeV/c < p < 200 MeV/c
(c) 200 MeV/c < p < 250 MeV/c (d) 250 MeV/c < p < 300 MeV/c

seen. Finally, there are a number of electrons with LA energy roughly equal to their momenta. Clearly, however, the identification of a large number of particles would be ambiguous on the basis of total energy alone.

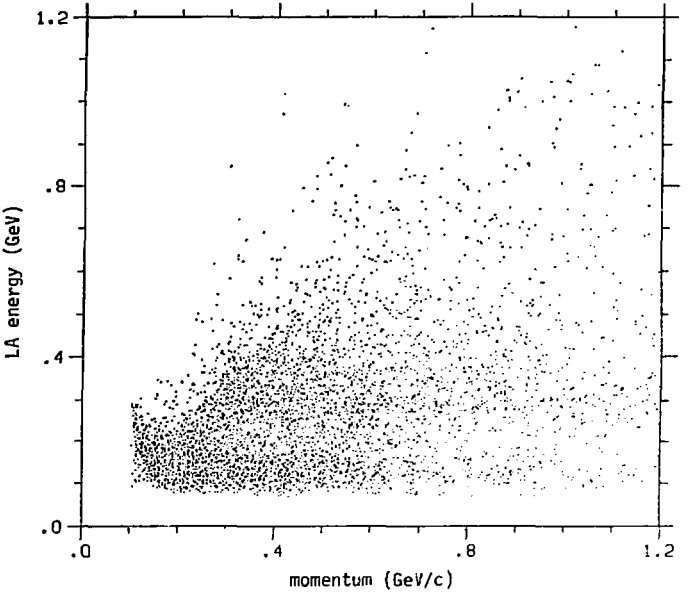

Figure 28: Liquid argon energy vs. momentum

electrons and pions in antiproton events with E_{cm} > 4.5 GeV

5.2.2 Electron Identification Efficiency

The efficiency of the electron identification procedure for correctly identifying real electrons was determined by analyzing two different samples of electrons —

1) Photon conversions $\gamma \rightarrow e^+e^-$

Photon conversions in the pipe counter provide a source of real electrons which can be identified without using TOF or LA information. Reconstruction of a secondary vertex at the pipe counter radius (12 cm), consisting of two oppositely charged tracks with small opening angle, is sufficient to identify photon conversions with little background from chance track crossings. A collection of 10000 e^+e^- pairs identified in this manner was passed through the regular electron identification procedure to determine the electron identification efficiency.

2) Monte Carlo generated electrons

The Mark II Monte Carlo program HOWL was used to generate 8000 electrons with momentum from 200 to 300 MeV/c and 7000 electrons with momenta from 300 MeV/c to 1200 MeV/c. The Monte Carlo program generated raw data (DC hits, TOF measurements, LA pulseheights, etc.), which were then passed through the same analysis program used for real data. Bremsstrahlung, energy loss, and multiple Coulomb scattering in the material preceding the drift chamber are incorporated into the Monte Carlo. A Gaussian TOF resolution of 300 ps was used. Electromagnetic showers were generated for electrons with mo-

mentum greater than 300 MeV/c by the shower simulation program EGS [19]. This program tracks the cascade of electrons and photons produced by an incident electron through a liquid argon module, depositing the appropriate amount of ionization energy in the liquid argon gaps as they are crossed. The accuracy of the Monte Carlo shower generation program has been verified for high energy electrons from Bhabha scattering and for low energy electrons from photon conversions.

The results of these two methods of determining the electron detection efficiency are collected in table 6. In each column, the numbers shown represent the effect only of the final electron selection cut (TOF electron weight greater than 0.9 for momentum less than 300 MeV/c or LAESEP electron probability greater than 0.9 for momentum greater than 300 MeV/c). The complete electron detection efficiency is obtained by including the solid angle, time-of-flight and liquid argon quality, and distance of closest approach efficiencies previously discussed, plus a pair mass efficiency to be discussed later. For the actual efficiency correction, the numbers shown in table 6 were smoothed by fitting them to exponential functions of momentum in the separate momentum ranges 150-300 MeV/c and 300-1200 MeV/c. The resulting efficiencies are collected in the last column of table 6. In this column, the number in parenthesis is the total electron efficiency, including all corrections. The total electron detection efficiency (measured data points along with smooth fit) is plotted in figure 29. Systematic errors in the overall efficiency are estimated to be less than 2 % over most of the momentum range, based on the good agreement between the two separate efficiency measurements.

TABLE 6

Electron detection efficiency

p(MeV/c)	- Method of Determination - Photon conversion	Monte Carlo	Efficiency (from fit)
150-175	.994 ± .002	1.00	.99 (.62 ± .02)
175-200	.975 ± .004	.983 ± .007	.97 (.60 ± .02)
200-225	.941 ± .007	.931 ± .007	.93 (.58 ± .02)
225-250	.842 ± .012	.840 ± .010	.86 (.53 ± .02)
250-275	.755 ± .015	.715 ± .015	.75 (.47 ± .02)
275-300	.663 ± .018	.604 ± .016	.61 (.38 ± .02)
300-400	.679 ± .011	.627 ± .018	.65 (.36 ± .02)
400-500	.708 ± .015	.676 ± .017	.69 (.38 ± .02)
500-600	.718 ± .019	.716 ± .018	.73 (.40 ± .02)
600-700	.781 ± .023	.764 ± .017	.75 (.41 ± .02)
700-900	.767 ± .022	.754 ± .018	.76 (.42 ± .02)
900-1200	.823 ± .026	.757 ± .016	.78 (.43 ± .02)

The errors in the first two columns are statistical only. Systematic errors are included in the final column.

The final number (in parenthesis) includes efficiency factors for solid angle, time-of-flight and liquid argon quality, distance of closest approach, and pair mass cuts totaling :

$(.75)(.87)(.98)(.97) = .62$ for $p < 300$ MeV/c
$(.64)(.88)(.98)(.99) = .54$ for $p > 300$ MeV/c

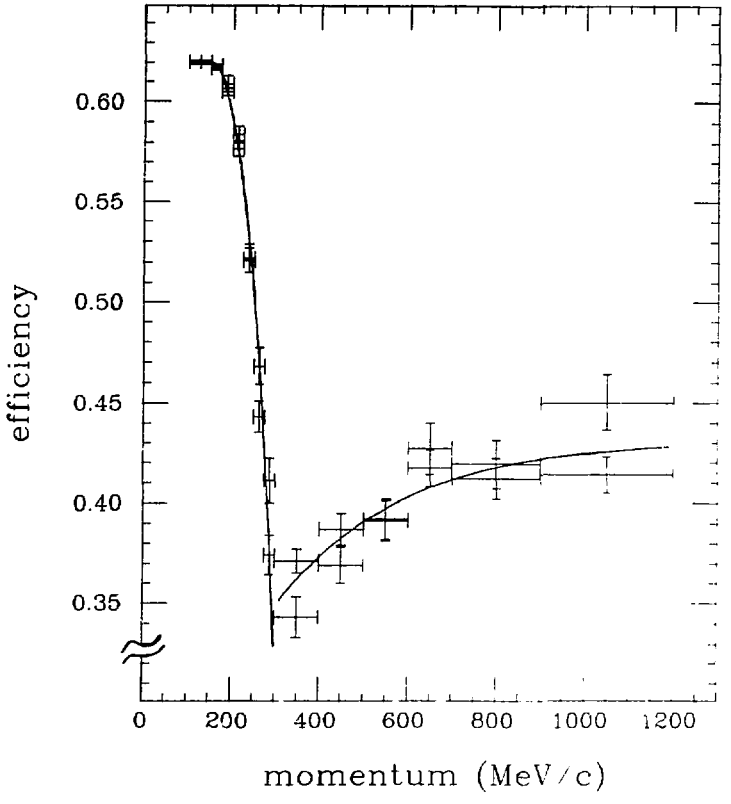

Figure 29: Electron detection efficiency

5.2.3 Charged Pion Misidentification

Charged pions misidentified as electrons are the most serious background in this analysis. There are more misidentified pions than real electrons in the baryon event sample, so the background subtraction introduces large statistical errors. It is important to determine precisely the level of pion contamination in the electron sample in order to perform an accurate subtraction.

The probability of misidentifying a low momentum pion as an electron was determined from a sample of 15000 known pions from the decay $\psi' \rightarrow \psi\pi^+\pi^-$. This ψ' decay mode (branching ratio 33 %) is easily selected by plotting the invariant mass recoiling against an oppositely charged pair of low momentum tracks (assumed to be pions); a large narrow peak at the mass of the ψ is observed with little background, providing a clean signature for the above decay. The pions produced in this decay have a momentum spectrum peaked sharply at 200-300 MeV/c and were used to determine the probability of misidentifying a pion as an electron as a function of momentum below 300 MeV/c.

The pion misidentification probability is calculated as the fraction of pions which are called electrons by the final TOF weight cut, after having passed the previous TOF quality, distance of closest approach, and pair mass cuts required for all electron candidates with momentum less than 300 MeV/c. Table 7 gives the results of this calculation. Pion misidentification rises almost linearally with momentum, going from less than 1 % below 200 MeV/c to over 2 % at 300 MeV/c.

TABLE 7

Pion misidentification probability for p < 300 MeV/c

p(MeV/c)	$P^{meas}_{\pi\to e}$ (%)	$P^{fit}_{\pi\to e}$ (%)
100-125		
125-150		.25
150-175		.60
175-200	1.00±.24	.95
200-225	1.25±.25	1.30
225-250	1.60±.27	1.64
250-275	1.98±.30	1.99
275-300	2.40±.32	2.34

The above errors are statistical only, based on the size of the pion sample and the number of pions misidentified as electrons.

$$P^{fit}_{\pi\to e}(p) = -.0165 + .1391\ p\ (\mathrm{GeV/c})$$

for 100 MeV/c < p < 300 MeV/c

For the actual subtraction, the misidentification probabilities were fitted to a straight line, shown in table 7 and plotted in figure 30. The resulting misidentification probability curve, combined with the momentum spectrum of the identified pions in the data, was used to calculate the expected number of pions misidentified as electrons below 300 MeV/c.

The probability of misidentifying a high momentum pion as an electron was determined from a sample of 15000 known pions from the decays $\psi \to 2(\pi^+\pi^-)\pi^0$ and $\psi \to 3(\pi^+\pi^-)\pi^0$. These ψ decay modes (branching ratios 3.7 % and 2.9 % respectively) were selected by plotting the invariant mass recoiling against the four or six observed charged particles (as-

sumed to be pions); a peak is observed at the pizero mass, providing a clean signature for a decay with one missing neutral pion. Contamination of the pion sample by electrons from the decay $\psi \rightarrow e^+e^-e^+e^-$ was eliminated by removing events with recoil momentum near zero. The pions produced in these decays have a broad momentum spectrum peaked at about 400 MeV/c and extending to about 1200 MeV/c and were used to determine the probability of misidentifying a pion as an electron as a function of momentum above 300 MeV/c.

The pion misidentification probability is calculated as the fraction of pions which are identified as electrons by the final selection in LAESEP, after having passed the previous distance of closest approach, time-of-flight and liquid argon quality, and pair mass cuts required for all electron candidates with momentum greater than 300 MeV/c. Table 8 shows the probability of misidentifying a pion as an electron as determined from this pion sample. Pion misidentification is greater than 5 % at low momenta, where the ionization of the liquid argon caused by the electromagnetic shower of an electron is not much greater than the minimum ionization produced by a pion. As the pion momentum increases, the misidentification probability falls rapidly, dropping below 2 % at the highest momenta.

For the actual background subtraction, the misidentification probabilities were fitted to an exponentially decaying function, shown in table 8 and plotted in figure 30. The resulting smooth curves, combined with the momentum spectrum of the identified pions in the data, were used to calculate the expected numbers of pions misidentified as electrons above 300 MeV/c. An error was assigned to the calculated number of misidentified pions, based on the uncertainties in the measured pion misidentification probabilities shown in table 8.

TABLE 8

Pion misidentification probability for p > 300 MeV/c

p(MeV/c)	$P^{meas}_{\pi^-\to e^-}$ (%)	$P^{fit}_{\pi^-\to e^-}$ (%)	$P^{meas}_{\pi^+\to e^+}$ (%)	$P^{fit}_{\pi^+\to e^+}$ (%)
300-400	5.19±.73	5.22	7.18±.88	7.39
400-500	3.83±.63	3.72	5.93±.77	5.64
500-600	1.62±.43	2.78	4.32±.68	4.41
600-700	1.90±.51	2.19	3.96±.72	3.54
700-900	1.95±.41	1.70	2.36±.46	2.68
900-1200	1.27±.42	1.37	2.18±.56	1.96

The above errors are statistical only, based on the size of the pion sample and the number of pions misidentified as electrons.

$$P^{fit}_{\pi^-\to e^-} = .012 + .208\, e^{-4.72\, p\ (GeV/c)}$$

$$P^{fit}_{\pi^+\to e^+} = .014 + .201\, e^{-3.48\, p\ (GeV/c)}$$

There is a definite charge asymmetry in the pion misidentification probabilities above 300 MeV/c, where the electron identification relies on liquid argon information -- positive tracks are misidentified as electrons more often than are negative tracks. This asymmetry is believed to be due to charge exchange scattering in the lead - liquid argon modules. (Charge exchange scattering produces neutral pions which decay into photons, generating electromagnetic showers just like electrons. Since lead contains 50 % more neutrons than protons, π^+ Pb charge exchange scattering is more likely than π^- Pb charge exchange scattering.)

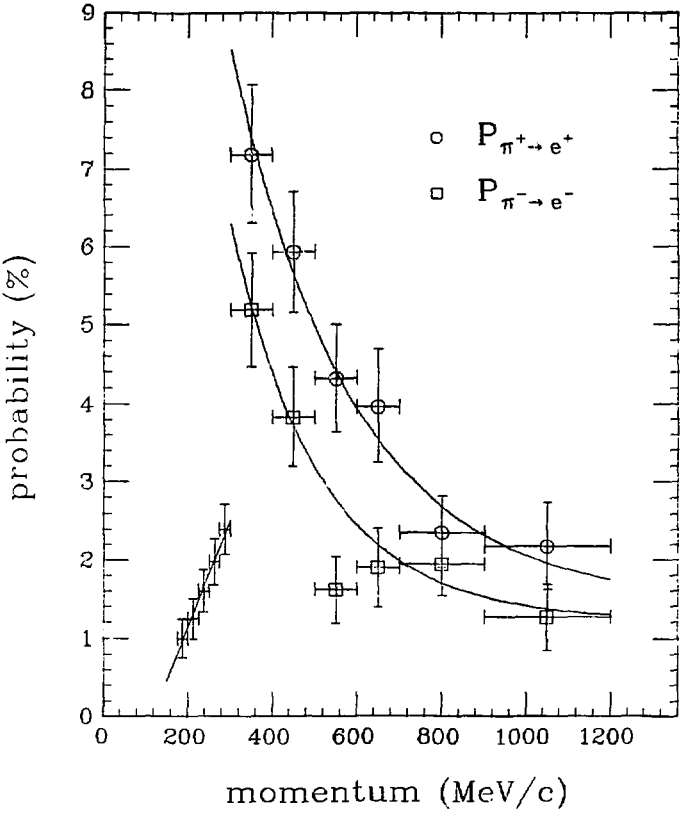

Figure 30: Pion misidentification probabilities

5.2.4 Electron - Positron Pairs from Pizero Decay

The second serious background in this analysis is real electron - positron pairs arising from photon conversions and Dalitz decays of pizeros. About one third of the electrons observed in the baryon event sample belong to e^+e^- pairs, so it is important to identify and remove as many of these unwanted electrons as possible. A statistical subtraction is necessary to correct for the remaining e^+e^- pairs which cannot be identified on an event by event basis.

Almost all photons in the data are themselves produced by pizero decay, so this background is proportional to the number of neutral pions in the data sample. To study this background source, a Monte Carlo calculation of pizero decays was performed. 17000 pizero tracks with momenta from 100 MeV/c to 1000 MeV/c were generated and allowed to decay either into two photons (98.85 % branching ratio) or into one photon and a Dalitz pair (1.15 % branching ratio). The photons were then allowed to convert into e^+e^- pairs. A conversion probability of 3.85 % was used, corresponding to the amount of material (.05 radiation length) in the vaccuum chamber and pipe counter assembly preceding the drift chamber. All photon conversions were generated at the pipe counter radius of 12 cm. The standard data analysis program was then run (using raw data generated by the Monte Carlo) to determine how often the produced electrons were detected. The following discussion is based on an examination of these events.

Depending on how well the electron and positron are tracked in the drift chamber, three distinct classes of e^+e^- pair events result.

These three classes of events require different treatment and are handled separately in the analysis, as described below.

1) Both electrons are tracked

If both electrons from an e^+e^- pair are tracked, the pair can be identified by its invariant mass. This is generally the case for electron pairs produced by pizeros with momentum greater than about 400 or 500 MeV/c. Unless the decay is quite asymmetric, both electrons will have sufficient momentum to be tracked in the drift chamber.

The invariant mass spectrum for these e^+e^- pairs peaks sharply at around 20-40 MeV/c^2; roughly 95 % of all e^+e^- pairs have invariant mass less than 60 MeV/c^2. In the real data analysis, candidate electrons were paired with all oppositely charged tracks in the event, and a 60 MeV/c^2 cut was made on the resulting invariant mass. A small inefficiency (1-3 %, depending on the electron momentum) is introduced by this procedure when good electrons happen to be produced nearly colinear to other charged tracks.

2) One electron is tracked and the other electron leaves a trail of drift chamber hits which the tracking program misses.

Asymmetric e^+e^- pairs frequently result in events with one tracked electron and one clearly visible track which is missed by the tracking program (usually because the momentum is very low). A hand scan of all electron tracks in the real data was used to eliminate probable e^+e^- pairs falling into this class. Usually the visual identification of an e^+e^- pair was unambiguous, but occasionally a guess had to be made; in such cases, I leaned toward eliminating dubious electrons. As long as the same criteria are used to identi-

fy this class of e^+e^- pair in both Monte Carlo events and in the real data, the final electron signal after the complete pizero background subtraction should be insensitive to the treatment of these ambiguous cases.

3) One electron is tracked and the other electron is not seen at all.

Electron - positron pairs in which one electron misses the drift chamber completely, having either very low momentum or small polar angle, result in a background which cannot be identified and eliminated on an event by event basis. A statistical subtraction, based on the pizero spectrum and the probability of a pizero to produce such a pair, is necessary.

The pizero spectrum in the real data was not directly measured, but was assumed to be the same as the measured charged pion spectrum, with normalization $N_{\pi^0} = \frac{1}{2}(N_{\pi^-} + N_{\pi^+})$. The Monte Carlo was used to construct a table of the probability for a pizero (of a given momentum) to produce an electron (of a given momentum), the other electron being unobserved. This table was then combined with the pizero spectrum to generate the expected spectrum of background electrons in the real data.

The spectrum of electrons from this class of pizero decay peaks at very low momentum. From 100-200 MeV/c, these electrons are the dominant source of background in the real data; by 300 MeV/c, they are far outnumbered in the real data by misidentified charged pions. In doing the background subtraction for electrons from this class of pizero decay, an error equal to 20 % of the subtraction itself was assigned, based on uncertainties in the Monte Carlo calculated probabilities for a pizero to produce one electron.

5.3 RESULTS

5.3.1 Electron Signal

Calculations of the final electron signals, including background subtractions and efficiency corrections, are presented in tables 9 - 12, which should be self-explanatory.

Below 4.5 GeV, the background subtraction should cancel the observed electron signal. In the lambda and antilambda events, the net electron signal after background subtraction is negative. In the antiproton events, the net electron signal after background subtraction is positive, at about the one standard deviation level. Above 4.5 GeV, the background subtraction leaves a net electron signal in both antiproton and lambda events, at about the three standard deviation level.

TABLE 9

Electron signal 9992 $\bar{p}$ events $E_{cm} < 4.5$ GeV

	identified electrons		background subtraction			efficiency corrected e	
p(MeV/c)	$N_{e^+}^{raw}$	$N_{e^-}^{raw}$	$N_{e^+}^{\pi^+}$	$N_{e^-}^{\pi^-}$	$N_{e^\pm}^{\pi^0}$	$N_{e^+}^{cor}$	$N_{e^-}^{cor}$
100-150	22	37	1	1	27	-9	15
150-200	26	38	7	7	22	-6	15
200-250	28	27	17	15	14	-6	-4
250-300	43	25	27	22	6	25	-6
300-400	123	81	129	72	2	-21	19
400-500	52	30	46	20	1	13	24
500-600	23	9	22	9		2	-1
600-700	22	3	11	4		26	-3
700-900	12	6	8	3		8	8
900-1200	3	3	2	1		1	5
	---	---	---	---	--	--	--
	354	259	270	154	72	34	71
	±19	±16	±19	±11	±8	±65	±43

total = 105 ± 78

$N_{e^\pm}^{raw}$ = number of identified electrons, with identified e^+e^- pairs removed

$N_{e^\pm}^{\pi^\pm}$ = number of electrons expected from misidentification of charged pions

$N_{e^\pm}^{\pi^0}$ = number of electrons (of each sign) expected from decays of neutral pions resulting in unidentified e^+e^- pairs

$N_{e^\pm}^{cor}$ = number of electrons after background subtraction and efficiency correction :

$$N_{e^\pm}^{cor} = (N_{e^\pm}^{raw} - N_{e^\pm}^{\pi^\pm} - N_{e^\pm}^{\pi^0}) / \text{eff}$$

TABLE 10

Electron signal 5209 $\bar{p}$ events E_{cm} > 4.5 GeV

	identified electrons		background subtraction			efficiency corrected e	
p(MeV/c)	$N_{e^+}^{raw}$	$N_{e^-}^{raw}$	$N_{e^+}^{\pi^+}$	$N_{e^-}^{\pi^-}$	$N_{e^\pm}^{\pi^0}$	$N_{e^+}^{cor}$	$N_{e^-}^{cor}$
100-150	12	17	0	0	15	-5	3
150-200	23	10	3	3	11	14	-7
200-250	11	20	7	6	9	-8	10
250-300	12	15	10	9	4	-6	5
300-400	69	42	68	37	2	-1	9
400-500	50	23	38	20	1	29	4
500-600	33	11	24	12		23	-1
600-700	23	11	14	6		21	12
700-900	17	18	12	7		11	27
900-1200	16	7	7	4		21	8
	---	---	---	---	--	--	--
	266	174	183	104	42	99	71
	±16	±13	±12	±7	±4	±45	±33

total = 170 ± 56

$N_{e^\pm}^{raw}$ = number of identified electrons, with identified e^+e^- pairs removed

$N_{e^\pm}^{\pi^\pm}$ = number of electrons expected from misidentification of charged pions

$N_{e^\pm}^{\pi^0}$ = number of electrons (of each sign) expected from decays of neutral pions resulting in unidentified e^+e^- pairs

$N_{e^\pm}^{cor}$ = number of electrons after background subtraction and efficiency correction :

$$N_{e^\pm}^{cor} = (N_{e^\pm}^{raw} - N_{e^\pm}^{\pi^\pm} - N_{e^\pm}^{\pi^0}) / eff$$

TABLE 11

Electron signal 1667 $\Lambda^0 + \bar{\Lambda}^0$ events $E_{cm} < 4.5$ GeV

	identified electrons		background subtraction			efficiency corrected e	
p(MeV/c)	$N^{raw}_{e^+}$	$N^{raw}_{e^-}$	$N^{\pi^+}_{e^+}$	$N^{\pi^-}_{e^-}$	$N^{\pi^0}_{e^\pm}$	$N^{cor}_{e^+}$	$N^{cor}_{e^-}$
100-150	5	4	0	.2	3.6	2.0	.2
150-200	3	9	.9	.7	3.1	-1.6	8.6
200-250	1	3	2.4	2.5	1.9	-5.8	-2.3
250-300	2	3	4.1	3.6	.5	-6.1	-2.6
300-400	9	11	13.1	12.0	.2	-12.1	-3.3
400-500	1	0	2.4	2.8		-3.6	-7.6
500-600	0	2	2.0	1.6		-4.8	.8
600-700	1	0	.6	.6		.9	-1.7
700-900	2	2	.5	.4		3.7	3.8
900-1200	0	0	.0	.0		-.3	-.2
	---	---	---	---	--	--	--
	24	34	26.2	24.5	9.4	-27.9	-4.2
	±4.9	±5.8	±1.9	±1.8	±1.0	±12.1	±13.6

total = -32 ± 18

Λ^0 and $\bar{\Lambda}^0$ events are combined in this table.

e^+ means [e^+ in Λ^0 events; e^- in $\bar{\Lambda}^0$ events] e^- means [e^- in Λ^0 events; e^+ in $\bar{\Lambda}^0$ events]

$N^{raw}_{e^\pm}$ = number of identified electrons, with identified e^+e^- pairs removed

$N^{\pi^\pm}_{e^\pm}$ = number of electrons expected from misidentification of charged pions

$N^{\pi^0}_{e^\pm}$ = number of electrons (of each sign) expected from decays of neutral pions resulting in unidentified e^+e^- pairs

$N^{cor}_{e^\pm}$ = number of electrons after background subtraction and efficiency correction :

$$N^{cor}_{e^+} = (N^{raw}_{e^+} - N^{\pi^\pm}_{e^+} - N^{\pi^0}_{e^+}) / \text{eff}$$

TABLE 12

Electron signal 837 $\Lambda^0 + \bar{\Lambda}^0$ events $E_{cm} > 4.5$ GeV

	identified electrons		background subtraction			efficiency corrected e	
p(MeV/c)	$N_{e^+}^{raw}$	$N_{e^-}^{raw}$	$N_{e^+}^{\pi^\pm}$	$N_{e^-}^{\pi^\pm}$	$N_{e^\pm}^{\pi^0}$	$N_{e^+}^{cor}$	$N_{e^-}^{cor}$
100-150	3	3	0	0	2.1	1.3	1.2
150-200	2	6	.3	.3	1.8	-.2	6.2
200-250	3	1	.8	1.1	1.4	-.5	-2.1
250-300	3	1	1.6	1.6	.5	2.3	-2.7
300-400	11	7	6.1	7.0	.1	13.3	-.7
400-500	5	4	4.4	4.5		1.3	-1.5
500-600	4	4	2.3	2.4		4.6	4.0
600-700	3	6	.9	1.2		4.8	11.8
700-900	2	4	1.6	1.4		.7	6.5
900-1200	1	1	.6	.2		.7	1.2
	---	---	---	---	--	--	--
	36	37	18.8	19.9	6.1	28.6	23.9
	±6.0	±6.1	±1.2	±1.3	±.6	±15.0	±13.6

total = 52 ± 20

Λ^0 and $\bar{\Lambda}^0$ events are combined in this table.

e^+ means [e^+ in Λ^0 events; e^- in $\bar{\Lambda}^0$ events] e^- means [e^- in Λ^0 events; e^+ in $\bar{\Lambda}^0$ events]

$N_{e^\pm}^{raw}$ = number of identified electrons, with identified e^+e^- pairs removed

$N_{e^\pm}^{\pi^\pm}$ = number of electrons expected from misidentification of charged pions

$N_{e^\pm}^{\pi^0}$ = number of electrons (of each sign) expected from decays of neutral pions resulting in unidentified e^+e^- pairs

$N_{e^\pm}^{cor}$ = number of electrons after background subtraction and efficiency correction :

$$N_{e^\pm}^{cor} = (N_{e^\pm}^{raw} - N_{e^\pm}^{\pi^\pm} - N_{e^\pm}^{\pi^0}) / \text{eff}$$

5.3.2 Electron Momentum Spectrum

The observed electron momentum spectra are plotted in figure 31 and tabulated in table 13.

TABLE 13

Electron momentum spectra $E_{cm} > 4.5$ GeV

p(MeV/c)	$\bar{p}$ events $N_{e^-} + N_{e^+}$	$\Lambda^0, \bar{\Lambda}^0$ events $N_{e^-} + N_{e^+}$
100-200	5 ± 14	8.8 ± 6.1
200-300	1 ± 17	-3.6 ± 6.1
300-400	8 ± 34	12.5 ± 12.6
400-500	33 ± 25	-.1 ± 6.9
500-600	22 ± 18	8.6 ± 7.7
600-700	34 ± 15	16.6 ± 7.3
700-900	39 ± 15	7.4 ± 5.9
900-1200	29 ± 12	1.9 ± 3.2

The lepton spectrum resulting from the decay of a charmed quark into a strange quark, a lepton, and a neutrino can be taken from the analogous QED calculation for muon decay. The result is

$$\frac{1}{\Gamma}\frac{d\Gamma}{dX} = \frac{12\, X^2\, [1-r^2-X]^2}{(1-X)} \qquad (0 \leq X \leq 1-r^2)$$

where $X = 2E / m_c$
r = quark mass ratio m_s/m_c
E = lepton energy in charmed quark rest frame

The lepton spectrum for the decay of a charmed baryon into a lambda, a lepton, and a neutrino is obtained by replacing the charmed quark mass by the charmed baryon mass and by replacing the strange quark mass by the lambda mass. This substitution increases r substantially but has little effect on the lepton spectrum except at the endpoint. Since the use of the actual baryon masses should more accurately reflect the kinematics of the Λ_c semileptonic decay, the higher value of r was used for comparison with the experimental lepton spectrum.

First order QCD corrections to the above formula, including real gluon bremsstrahlung and virtual gluon exchange, have been computed [20], but the resulting expressions are quite cumbersome. The gluon corrections turn out to give a large correction to the total semileptonic decay rate, but they do not appreciably change the shape of the lepton spectrum.

A correction to the lepton spectrum which is important is the transformation from the charmed quark rest frame to the e^+e^- rest frame. The experiment measures the lepton energy in the e^+e^- rest frame, where the produced charmed baryon has significant momentum. The laboratory momentum of the charmed baryon is shared by the charmed quark (apart from fermi motion of the quark within the baryon, which is a much smaller effect), and the boost this gives to the lepton emitted by the decaying quark can be quite large. The effect of this boost is to spread the lepton spectrum to higher momenta, while shifting the peak momentum slightly lower.

For a comparison with experiment, the theoretical lepton energy spectrum (expressed in terms of the lepton energy in the charmed quark rest frame) must be folded with the momentum distribution of the

charmed quark to give a corrected lepton energy spectrum (experessed in terms of the lepton energy in the lab frame). From the Lorentz transformation $E' = \gamma E (1 + \beta \cos\theta)$, the folding is done according to the formula

$$\frac{d\Gamma}{dE'} = \int_{-1}^{+1} d(\cos\theta) \left[\frac{d\Gamma}{dX} \bigg|_{X = \frac{2E'}{m_c\gamma(1+\beta\cos\theta)}} \right] \frac{1}{m_c\gamma(1+\beta\cos\theta)}$$

where β = velocity of charmed baryon (and charmed quark)
θ = angle between charmed baryon and lepton momenta
E' = lepton energy in lab frame

The integration was performed numerically, using as input the charmed baryon momentum distribution determined from the reconstructed hadronic decays $\Lambda_c \rightarrow pK\pi$. The corrected lepton spectrum is plotted in figure 31 as a solid curve, normalized to the number of electrons in the experimentally determined spectra. Within the large errors of the experimental spectra, the agreement is quite reasonable.

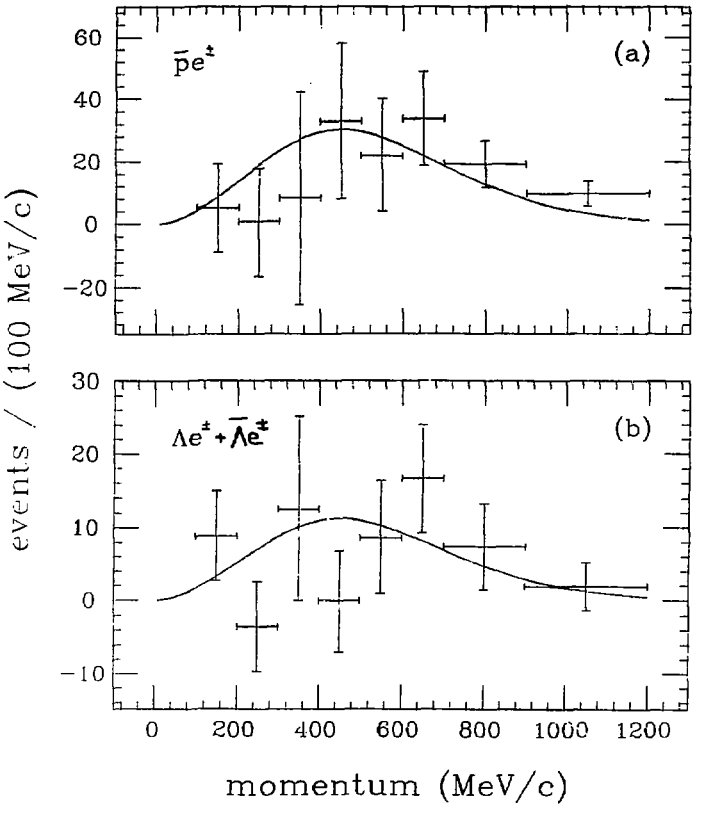

Figure 31: Electrom momentum spectra $E_{cm} > 4.5$ GeV

(a) antiproton events (b) lambda and antilambda events

5.3.3 E_{cm} Distribution of Electron Events

The distribution of electron events as a function of center-of-mass energy is plotted in figure 32 and tabulated in table 14. Subdividing the data results in very poor statistics, but the distributions are at least consistent with a threshold for electron production starting at around 4.5 GeV.

TABLE 14

E_{cm} distribution of electron events

E_{cm}(GeV)	N_{pe} / N_p (%)	$N_{\Lambda e}$ / N_Λ (%)
3.68	.9 ± .9	-1.7 ± 1.3
3.77	-1.0 ± 2.1	-7.3 ± 3.5
3.8-4.5	3.4 ± 2.3	-5.7 ± 3.9
4.5-5.1	4.2 ± 2.3	4.6 ± 5.3
5.1-5.3	3.0 ± 1.6	5.4 ± 3.8
5.3-6.2	5.7 ± 3.3	5.2 ± 8.6
6.2-6.8	2.1 ± 2.1	11.2 ± 6.0

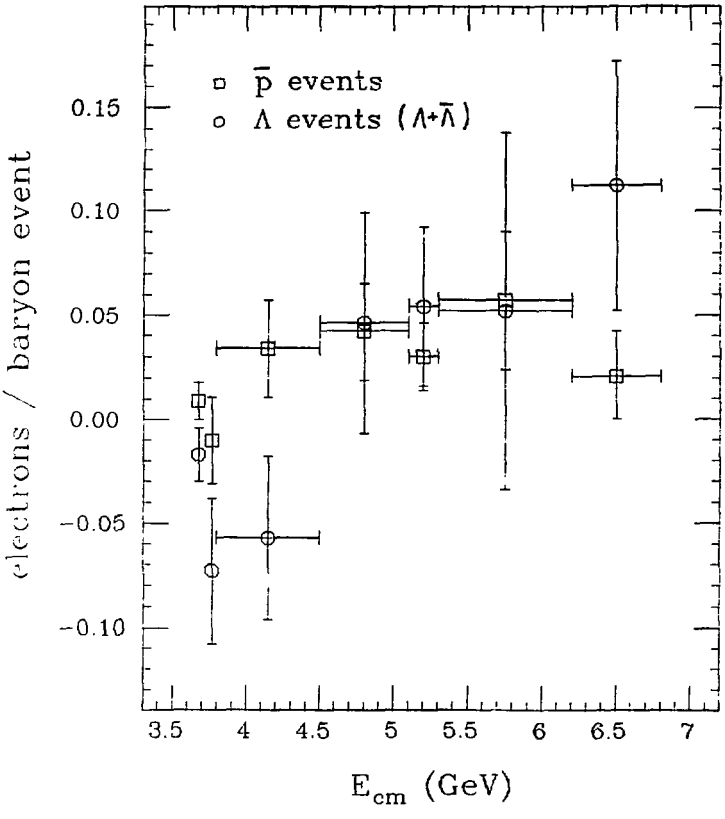

Figure 32: E_{cm} distribution of electron events

5.3.4 Electrons per Baryon Event

The basic results of these calculations are the fractions of baryon events above the charmed baryon threshold at 4.5 GeV containing a prompt electron or positron —

$$\frac{N(\bar{p}e^{+})}{N(\bar{p})} = \frac{(99\pm45)}{5209} = (\ 1.9 \pm 0.9\ )\ \%$$

$$\frac{N(\bar{p}e^{-})}{N(\bar{p})} = \frac{(71\pm33)}{5209} = (\ 1.4 \pm 0.6\ )\ \%$$

$$\frac{N(\bar{\Lambda}^{0}e^{+}) + N(\Lambda^{0}e^{-})}{N(\bar{\Lambda}^{0}) + N(\Lambda^{0})} = \frac{(23.9\pm13.6)}{(436+(.8)401)} = (\ 3.2 \pm 1.8\ )\ \%$$

$$\frac{N(\bar{\Lambda}^{0}e^{-}) + N(\Lambda^{0}e^{+})}{N(\bar{\Lambda}^{0}) + N(\Lambda^{0})} = \frac{(28.6\pm15.0)}{(436+(.8)401)} = (\ 3.8 \pm 2.0\ )\ \%$$

5.3.5 Semileptonic Branching Ratios

We assume that all events with both a baryon and an electron are events in which a charmed baryon - charmed antibaryon pair has been produced. In semileptonic decays of charmed baryons, the sign of the electron is correlated with the baryon number of the baryon — charmed baryons emit positrons, while charmed antibaryons emit electrons. Baryon - positron (and antibaryon - electron) events can be used to calculate the branching ratio of the charmed baryon into an electron plus the observed baryon. Baryon - electron (and antibaryon - positron) events, on the other hand, can be used to calculate the branching ratio of the charmed baryon into an electron plus any baryon. In this second case, the observed baryon is not associated with the observed semileptonic decay and serves only as a tag for a charmed baryon event.

To calculate semileptonic branching ratios from the measured numbers of baryon events containing electrons, an estimate of the charmed baryon content of the proton and lambda data samples is needed. For this purpose, the Mark II measurements of inclusive proton and lambda production, R_p and R_Λ as functions of E_{cm}, are used. Assuming that the increase in R_p (R_Λ) observed at center-of-mass energies greater than the threshold at 4.5 GeV is due entirely to charmed baryon pair production, the fractional increase in R_p (R_Λ) at a given center-of-mass energy gives the fraction of proton (lambda) events at that energy due to charmed baryon production and decay. Table 15 gives the measured values of R_p and R_Λ (calculated from the data presented in chapter 3) and the resulting values of $\Delta R_p/R_p$ and $\Delta R_\Lambda/R_\Lambda$ for the broad E_{cm} bins used in this analysis. The average values of $\Delta R_p/R_p$ and $\Delta R_\Lambda/R_\Lambda$, weighted by

the numbers of baryon events in each E_{cm} bin, are included in table 15 and used in the actual calculations.

TABLE 15

ΔR_p / R_p and ΔR_Λ / R_Λ

E_{cm} (GeV)	$R_p + R_p$	$\Delta R_p/R_p$	$R_\Lambda + R_\Lambda$	$\Delta R_\Lambda/R_\Lambda$
3.8 - 4.5	.36	-	.059	-
4.5 - 5.1	.49	.27	.097	.39
5.1 - 5.3	.67	.46	.133	.55
5.3 - 6.2	.70	.48	.145	.59
6.2 - 6.8	.79	.54	.205	.71
weighted average	.68	.45	.148	.57

$\Delta R_p(E_{cm}) = R_p(E_{cm}) - R_p(3.8\text{-}4.5)$
$\Delta R_\Lambda(E_{cm}) = R_\Lambda(E_{cm}) - R_\Lambda(3.8\text{-}4.5)$

A final number needed for some of the semileptonic branching ratio calculations is the fraction of charmed baryon decays (F_p) which lead to a proton (rather than a neutron) as the final state baryon. As in the calculation of the total charmed baryon cross section in chapter 3, the value $F_p = 0.6$ is taken here. The fraction of charmed baryon decays (F_Λ) which lead to a lambda in the final state may be calculated from F_p and the ratio $\Delta R_\Lambda/\Delta R_p$; using $\Delta R_\Lambda/\Delta R_p = 0.32$ (averaged over center-of-mass energies from 4.5 to 6.8 GeV) gives $F_\Lambda = 0.19$.

The calculations of the various semileptonic branching ratios of the charmed baryon proceed as follows :

$$BR\ (\ \Lambda_c^+ \rightarrow e^+\ X\ ) \ = \ \frac{N(\bar{p}e^+)}{N(\bar{p})} \left[\frac{\Delta R_p}{R_p} \right]^{-1} = \ (\ 4.2 \pm 1.9\ )\ \%$$

$$BR\ (\ \Lambda_c^+ \rightarrow e^+\ X\ ) \ = \ \frac{N(\bar{\Lambda}^0 e^+)+N(\Lambda^0 e^-)}{N(\bar{\Lambda}^0)+N(\Lambda^0)} \left[\frac{\Delta R_\Lambda}{R_\Lambda} \right]^{-1} = \ (\ 5.4 \pm 3.1\ )\ \%$$

Averaging these two results gives $BR\ (\ \Lambda_c \rightarrow e^+\ X\ ) = (\ 4.5 \pm 1.8\ )\ \%$.

$$BR\ (\ \Lambda_c^+ \rightarrow p\ e^+\ X\ ) \ = \ \frac{N(\bar{p}e^-)}{N(\bar{p})}\ (F_p) \left[\frac{\Delta R_p}{R_p} \right]^{-1} = \ (\ 1.9 \pm 0.8\ )\ \%$$

$$BR\ (\ \Lambda_c^+ \rightarrow \Lambda^0\ e^+\ X\ ) = \ \frac{N(\bar{\Lambda}^0 e^-)+N(\Lambda^0 e^+)}{N(\bar{\Lambda}^0)+N(\Lambda^0)}\ (F_\Lambda) \left[\frac{\Delta R_\Lambda}{R_\Lambda} \right]^{-1} = (\ 1.2 \pm 0.6\ )\ \%$$

Note that protons from secondary decays of lambdas are included in $BR(\Lambda_c \rightarrow peX)$ and lambdas from secondary decays of sigmas are included in $BR(\Lambda_c \rightarrow \Lambda^0 eX)$.

The only significant error in these calculations is the statistical uncertainty in the number of electron events. Errors in the values of $\Delta R_p/R_p$ and $\Delta R_\Lambda/R_\Lambda$ and in the values of F_p and F_Λ are much smaller and have been neglected.

5.3.6 Λ_c lifetime

The inclusive semileptonic branching ratio $BR(\Lambda_c \to eX)$ can be related to the Λ_c lifetime if the Λ_c semileptonic width is known. The theoretical result for the semileptonic width of a free charmed quark is [21]

$$\Gamma_{SL} = (G^2/192\pi^3)\, m_c\, g(r)\, [1-(2\alpha_s/3\pi) f(r)]$$

where r is the quark mass ratio m_s/m_c
$g(r)$ is a kinematic correction for the nonzero s quark mass
$f(r)$ is a QCD correction for real and virtual gluon exchange

The value of Γ_{SL} clearly depends critically on the charmed quark mass. The best determination of the charmed quark mass comes from fits to the lepton energy spectrum observed in semileptonic D decay [22], which give $m_c = (1.75 \pm 0.10)$ GeV/c^2. Using this value, the theoretical semileptonic width becomes

$$\Gamma_{SL} = (1.9 \pm 0.5)\cdot 10^{11}\ \mathrm{sec}^{-1} \qquad \text{for } m_c = (1.75 \pm .10)\ \mathrm{GeV}/c^2 .$$

Together with the experimentally measured branching ratio $BR(\Lambda_c \to eX) = (4.5 \pm 1.8)$ % from the present analysis, this gives a charmed baryon lifetime

$$\tau(\Lambda_c) = BR(\Lambda_c \to eX) / \Gamma_{SL} = (2.4 \pm 1.1)\cdot 10^{-13}\ \mathrm{sec}.$$

This result is in good agreement with direct measurements of the Λ_c lifetime [23], which give

$$\tau(\Lambda_c) = (1.7^{+0.9}_{-0.5})\cdot 10^{-13}\ \mathrm{sec}.$$

REFERENCES

1. The classic paper here is :
   Gaillard, Lee, and Rosner, Rev. Mod. Phys. 47 (1975) 277.

2. Mass estimates have been computed by many people; those quoted here are taken from :
   Korner, Kramer, and Wildrodt, Z. Physik C2 (1979) 117.

3. De Rujula, Georgi, and Glashow, Phys. Rev. D12 (1975) 147;
   Knapp et al, Phys. Rev. Lett. 37 (1976) 882.

4. Cazzoli et al, Phys. Rev. Lett. 34 (1975) 1125;
   Calicchio et al, Phys. Lett. 93B (1980) 521;
   Baltay et al, Phys. Rev. Lett. 42 (1979) 1721.

5. Glashow, Iliopoulos, and Maiani, Phys. Rev. D2 (1970) 1285.

6. Brandelik et al, Phys. Lett. 70B (1977) 125,387;
   Feller et al, Phys. Rev. Lett. 40 (1978) 1677;
   Kirkby, SLAC-PUB-2419 (invited talk at IX Int. Symp. on Lepton and Photon Int., Batavia, Il. 1979).

7. Korner, Kramer, and Wildrodt, Phys. Lett. 78B (1978) 492.

8. Lee, Quigg, and Rosner, Phys. Rev. D15 (1977) 157.

9. Buras, Nucl. Phys. B109 (1976) 373.

10. Pacheco, Grifols, and Ferreira, Lett. Nuovo Cimento 20 (1977) 303.

11. Schindler, PhD. Thesis (Stanford), SLAC Report 219 (1979).

12. Willis and Radeka, Nucl. Inst. Meth. 120 (1974) 221.

13. Dorfan, Mark II internal memorandum (4/4/1979);
    Friedman, IEEE Transactions on Computers (1977) 404.

14. Abrams et al, Phys. Rev. Lett. 44 (1980) 10.

15. Brandelik et al, Nucl. Phys. B148 (1979) 189.

16. Coles, PhD. Thesis (Berkeley), LBL-11513 (1980).

17. Feldman, Mark II internal memo (7/24/1979);
    Peshkin and Rosner, Nucl. Phys. B122 (1977) 144.

18. Abrams et al, Phys. Rev. Lett. 44 (1980) 10;
    Weiss, SLAC-PUB-2558 (invited talk at IV Int. Conf. on Baryon Resonances, Toronto, Canada, 1980).

19. Ford and Nelson, EGS code, SLAC Report 210 (1978).

20. Ali and Pietarinen, Nucl. Phys. B154 (1979) 519;
Cabibbo, Corbo, and Maiani, Nucl. Phys. B155 (1979) 93.

21. Cabibbo and Maiani, Phys. Lett. 79B (1978) 109.

22. Ali and Pietarinen, Nucl. Phys. B154 (1979) 519;
Cabibbo, Corbo, and Maiani, Nucl. Phys. B155 (1979) 93.

23. Prentice, invited talk at Rencontre de Moriond, Les Arcs, France (1981);
Ushida et al, Phys. Rev. Lett. 45 (1980) 1053.